Penetration of mantle plumes through depleted lithosphere

D. Jurine, C. Jaupart, G. Brandeis, P. Tackley

▶ **To cite this version:**

D. Jurine, C. Jaupart, G. Brandeis, P. Tackley. Penetration of mantle plumes through depleted lithosphere. Journal of Geophysical Research : Solid Earth, 2005, 110 (B10), pp.B10104. 10.1029/2005JB003751 . insu-02920427

Penetration of mantle plumes through depleted lithosphere

D. Jurine, C. Jaupart, and G. Brandeis

Laboratoire de Dynamique des Systèmes Géologiques, Institut de Physique du Globe de Paris, Paris, France

P. J. Tackley

Department of Earth and Space Sciences and Institute of Geophysics and Planetary Physics, University of California, Los Angeles, California, USA

[1]   Laboratory experiments and numerical calculations are used to study how a laminar thermal plume deforms and penetrates a buoyant and viscous layer, which serves as an analog for continental lithosphere. The viscosity contrast between the two liquids and the buoyancy ratio B (the ratio between the intrinsic chemical density contrast and the thermal density contrast due to temperature differences) are varied by 3 orders of magnitude and 1 order of magnitude, respectively. The manner of plume-lithosphere interaction is not sensitive to the viscosity contrast, which sets the timescale for displacement of the interface, and depends mostly on the B value, which sets the magnitude and shape of interface deformation. Heating of the upper layer by plume material plays an important role. For $B > 0.6$, plume material spreads beneath the interface and applies a buoyancy force which deforms the interface. For $B < 0.6$, true plume penetration into the upper layer occurs with a significant vertical velocity component. With time, the upper layer may become unstable and develop an active upwelling which entrains material from the lower layer. Approximate scaling laws allow prediction of interface displacement as a function of time for the whole parameter range studied. Applied to the continental lithosphere, these results show that true plume penetration through Archean lithosphere requires thermal anomalies larger than 300 K corresponding to buoyancy fluxes in excess of those determined today for the Hawaiian plume. Mantle plumes have different effects on lithospheres of different ages and composition, which precludes diagnosis of a single "typical" plume signature.

Citation: Jurine, D., C. Jaupart, G. Brandeis, and P. J. Tackley (2005), Penetration of mantle plumes through depleted lithosphere, *J. Geophys. Res.*, *110*, B10104, doi:10.1029/2005JB003751.

1. Introduction

[2] Mantle plumes, an unavoidable feature of high Rayleigh number convection, were first brought to the fore by *Morgan* [1971] in his study of oceanic hot spots. Since then, they have been held responsible for a large variety of geological phenomena, including flood basalts, kimberlite fields and the voluminous melting events which predate continental rifting. They have also been invoked to account for the very process of continental growth in the Archean. This wealth of attributes, together with the difficulty to detect the expected temperature anomalies over large depth extents in the convecting mantle, have led many authors to question the geological relevance of mantle plumes and even their existence. Part of the problem may be that for lack of unambiguous direct geophysical evidence, plumes are only defined by near-surface effects, i.e., by the way they interact with the

lithosphere. Two recent reviews emphasize that our current understanding of basic plume physics is sound and comprehensive [*Jellinek and Manga*, 2004; *Ribe et al.*, 2005] but also that little has been done on plume-lithosphere interaction. This deficiency is blatant when one factors in the fact that continental and oceanic lithospheres differ by their bulk composition and intrinsic buoyancy. The problem of plume-lithosphere interaction must be posed as that of plume behavior at a density and viscosity interface, with jumps in density and viscosity varying from case to case. One justification for our analysis comes from *Turner et al.* [1996], who have shown that there is more than one type of continental flood basalt. The Deccan Traps, India, were probably derived by decompression melting of asthenospheric mantle in contrast to the Paraná, Brazil, where basalts bear the geochemical signature of subcontinental lithospheric mantle. This difference may be attributed to changes in the relative importance of two mechanisms, heating of the lithosphere by a plume and lithospheric stretching driven by far-field tectonic forces [*White and McKenzie*, 1989; *Huismans et al.*, 2001]. Here, we propose

an alternative explanation involving a comparison between the intrinsic buoyancy of continental material and thermal buoyancy of heated asthenosphere.

[3] Many studies of plume-lithosphere interaction have neglected plume penetration through the lithosphere and have focused on the ponding and lateral spreading of buoyant material at the base of a rigid lid [Olson et al., 1988; Griffiths and Campbell, 1991; Sleep, 1994; Kerr and Mériaux, 2004]. Yet high-resolution numerical studies indicate that thinning of the lithosphere may proceed at geologically significant rates [Moore et al., 1999; Vezolainen et al., 2003]. It is difficult to compare these various results, partly because they rely on different models of the lithosphere and partly because they are not scaled as a function of lithosphere properties and plume characteristics.

[4] Geophysical studies reveal lithospheric anomalies associated with large magmatic events. For example, Bank et al. [1998] have determined the presence of a pronounced low-velocity anomaly of small width (120 km) through the lithospheric mantle beneath the south central Saskatchewan kimberlite field, Canada, and have suggested that it is due to thermomechanical erosion of the lithospheric keel. Similar anomalies have been found beneath the Monteregian– White Mountain–New England hot spot track in northeastern America or beneath the Bushveld intrusion in South Africa [Rondenay et al., 2000; Fouch et al., 2004]. Interpreting these anomalies requires some knowledge of the physical controls on the extent of plume penetration and lithosphere deformation.

[5] In this paper, we study how thermal plumes interact with viscous and buoyant layers which serve as analogs for continental and oceanic lithospheres of various ages. The lithosphere-like layer is more viscous and intrinsically less dense than the underlying liquid. A thermal plume is generated at the base of the lower liquid. We observe how the lithosphere-like layer deforms and gets penetrated by the plume over a large range of plume buoyancy fluxes, lithosphere intrinsic densities, viscosities and thicknesses. A key parameter is the buoyancy ratio B, which is the ratio of the intrinsic density difference due to composition, $\Delta\rho_c$ to the thermal density difference due to the plume temperature anomaly, $\Delta\rho_T$. Here, B was varied from small values (≈ 0.2), such that upward plume penetration is extensive, to values as large as 3, such that the plume does not really penetrate into the layer but only acts to heat up its base. Laboratory experiments and numerical calculations are both used to study in detail the shape and dimensions of the induced lithosphere deformation. Approximate scaling laws are derived for interface deformation.

2. Model System

2.1. Geophysical Constraints

[6] The continental and oceanic lithospheres differ from one another by their thickness and chemical composition [Boyd, 1989]. Oceanic lithosphere thickness varies as a function of age with a maximum of about 100 km, whereas continental lithosphere is probably as thick as 250 km beneath Archean cratons [Jaupart and Mareschal, 1999; Rudnick and Nyblade, 1999; Gung et al., 2003]. The density of the subcontinental lithospheric mantle has been determined directly using xenoliths and appears to vary with age,

from a value of 3.31 ± 0.02 Mg m^{-3} for the Archean to 3.36 ± 0.02 Mg m^{-3} for the Phanerozoic. In comparison, the density of the underlying convecting mantle is estimated to be 3.39 Mg m^{-3} assuming "primitive mantle" composition [Poudjom-Djomani et al., 2001]. These results indicate the continental lithosphere is intrinsically buoyant (i.e., because of its chemical composition) with respect to the convecting mantle down to its base, a result confirmed by gravity and geoid studies [Doin et al., 1996]. The intrinsic buoyancy, defined as $\Delta\rho_c/\rho_0$, where $\Delta\rho_c$ is the chemical density difference and ρ_0 a reference density, takes values between about 1% and 3%. The oceanic lithosphere has also been depleted by melt extraction, and its intrinsic buoyancy is about 1% [Oxburgh and Parmentier, 1977; Morgan, 1997]. A plume rising from depth thus encounters intrinsically buoyant material beneath both continents and oceans, but the intrinsic buoyancy and lithosphere thickness vary from case to case.

[7] Mantle plume thermal anomalies have been calculated with various methods and estimates vary between $\Delta T \approx 50$ to $\Delta T \approx 300$ K [Sleep, 1990; Albers and Christensen, 1996; Ribe and Christensen, 1999]. Such plumes need first to rise through the convective boundary layer at the base of the lithosphere, across which there is a temperature difference of about 200 K [Jaupart et al., 1998]. Thus the plume thermal anomaly at the base of the lithosphere lies in a 200– 500 K range. For a thermal expansion coefficient of 4×10^{-5}, one has therefore $0.8\% < \Delta\rho_T/\rho_o < 2\%$. The relevant parameter to compare intrinsic and thermal buoyancy is the buoyancy ratio B:

$$B = \frac{\Delta\rho_c}{\Delta\rho_T}. \tag{1}$$

B takes a typical value of about 1 for Archean lithosphere and may be as small as 0.5 for Phanerozoic continental lithosphere and oceanic lithosphere.

[8] The rheological properties of lithospheric mantle are very sensitive to the water content. Both continental and oceanic lithospheric mantles have been dehydrated by partial melting and hence are more viscous than the underlying asthenospheric mantle [Kohlstedt et al., 1995]. The viscosity contrast is probably within a range of 1–2 orders of magnitude [Hirth and Kohlstedt, 1996], which is required for long-term stability of continental lithosphere [Doin et al., 1997; Lenardic and Moresi, 1999].

2.2. Model System and Methods

[9] Posed in the most general terms, plume-lithosphere interactions involves many different processes, physical properties and variables. We study a simplified system such that a plume rises through a fluid layer and penetrates through an upper layer made of buoyant and more viscous material. Both fluid layers are isoviscous. Before plume initiation, the two layers are isothermal and all subsequent temperature anomalies are due to the plume. Even such a "bare bones" model problem introduces as many as five different dimensionless numbers. The advantage of simplifying the problem is that control variables and processes can be analyzed clearly. In geological reality, the upper layer (the lithosphere) is thermally and rheologically stratified [Jaupart et al., 1998; Solomatov and Moresi, 2000]. It may
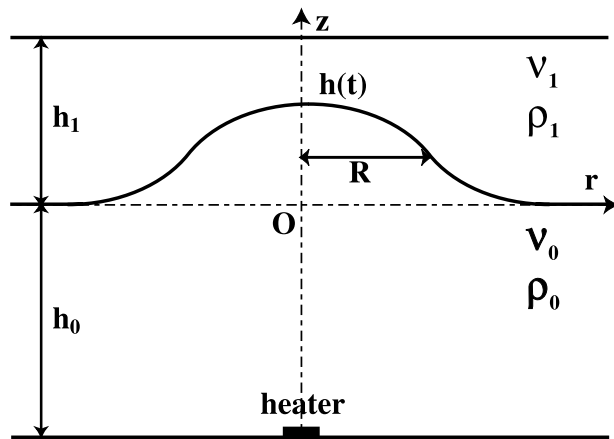
Figure 1. Model system of two layers with a basal heat source to generate a thermal plume. The plume induces deformation of the interface between the two layers; $h(t)$ denotes the maximum interface displacement at the axis.

also develop complex compositional stratification due to several accretion events, as in the Archean Slave province, Canada [*Aulbach et al.*, 2004]. Another complication is that continental lithosphere may be refertilized by metasomatic fluids [*Griffin et al.*, 2003]. For these reasons, it is valuable to develop compact scaling laws allowing rapid comparisons of different cases. We studied viscosity contrasts as large as 10^3, which is above that due to dehydration [*Hirth and Kohlstedt*, 1996], in order to approximate additional effects of temperature stratification. We discuss how the simplifying assumptions affect our results in section 5.

[10] Let us consider a stratified system with a bottom layer of thickness h_0, density ρ_0 and viscosity ν_0, supposed to represent Earth's asthenosphere, lying below an upper layer made of a different material, with thickness h_1, density ρ_1 and viscosity ν_1, such that density $\rho_1 < \rho_0$ and $\nu_1 > \nu_0$ (Figure 1). The plume is characterized by its energy flux Q, proportional to its buoyancy flux, and its source depth. The problem involves flow in two chemically distinct fluids and deformation of a material interface, as well as convection phenomena on different scales. Numerical methods require a large number of grid points to allow proper resolution of the small-scale structure of thermal boundary layers, as well as material points (tracers) to follow the interface between the two fluids. Limitations of computing power and memory do not allow extensive resolution tests. For this reason, we have also carried out laboratory experiments and compare them to numerical results. Experiments have their own limitations, and numerical results are needed to study a large range of parameters. The tracer method has been bench marked with different codes [*van Keken et al.*, 1997; *Tackley and King*, 2003] but has not been compared to laboratory experiments. As discussed in Appendix C, the present problem involving thermal plumes rising through a layered system offers a stringent test.

[11] In the laboratory, a plume is generated by ohmic dissipation in a small electrical coil at the base of a tank. In the numerical calculations, a uniform heat flux is imposed over a small area at the base of the computational domain. Although it is straightforward to impose the same energy

flux in both, it is difficult to achieve the same plume characteristics over a rather small study volume. In both cases, the source has finite dimensions and it is impossible to achieve the same initial distribution of heat flux density. For this reason, the proper way to characterize a thermal plume is to refer to a virtual point source located at some depth below the true source (Figure 2). Proper comparison can then be made between laboratory experiments and numerical calculations with a (virtual) point source located at the same depth beneath the interface and supplying the same energy flux. As discussed in Appendix C, for the same source location and same energy flux, axial plume temperature anomalies in laboratory experiments and numerical calculations differ by about 10%. This small difference may be attributed to the small distance from source and has little impact on the end results. Details can be found in Appendix C.

2.3. Dimensional Analysis

[12] The equation of state for the two fluids is

$$\rho_i(T) = \rho_i(1 - \alpha T), \ i = 0, 1, \tag{2}$$

where we have assumed that expansion coefficient α is the same for both fluids, which is appropriate for both the true geological system and the experimental setup.

[13] When it reaches the interface, the plume temperature is larger than in the surrounding liquid by an amount ΔT. For energy flux Q, at distance z above source, the thermal anomaly is spread over a radius which is proportional to scale R_θ [*Batchelor*, 1954; *Moses et al.*, 1993; *Kaminski and Jaupart*, 2003]:

$$R_\theta = \left[\frac{\kappa z}{\sqrt{g\alpha Q/\rho C_p \nu_0}} \right]^{1/2}. \tag{3}$$

ΔT and R_θ provide scales for temperature and length. The true width of the thermal anomaly is larger than R_θ by a large factor (about 4). We shall see that in fact, the details of plume penetration are not sensitive to this length scale
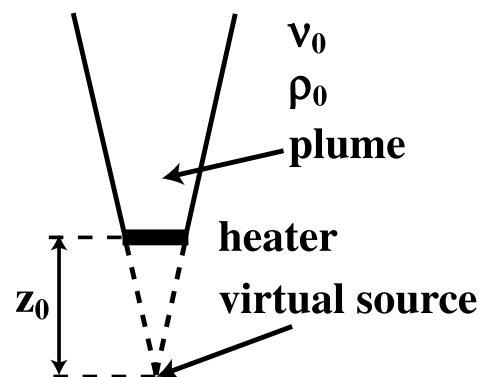

Figure 2. Schematic diagram showing how a plume generated by heating over a finite lateral distance can be referred to a virtual point source located below the heater. Laboratory experiments and numerical calculations are set up so that they have the same virtual point source and power input.

because the plume spreads over a large horizontal distance. The velocity scale W_0 is

$$W_0 = \frac{Q}{\rho C_p \Delta T R_\theta^2} . \qquad (4)$$

We further obtain a timescale and a pressure scale:

$$\tau = \frac{R_\theta}{W_0} = \frac{\rho C_p \Delta T R_\theta^3}{Q} \qquad (5)$$

$$\mathcal{P} = \frac{\mu_1 W_0}{R_\theta} . \qquad (6)$$

We define the stabilizing chemical density difference and the destabilizing thermal density difference as

$$\Delta \rho_c / \rho_0 = \frac{\rho_0 - \rho_1}{\rho_0} \qquad (7)$$

$$\Delta \rho_T / \rho_0 = \frac{\rho_0(T_o) - \rho_0(T_o + \Delta T)}{\rho_0} = \alpha \Delta T. \qquad (8)$$

[14] The origin of the coordinate system is fixed at the initial interface, such that $z < 0$ in the lower layer. Boundary conditions are a rigid lower boundary and a free-slip upper boundary. In the numerical calculations, the top and bottom boundaries are kept at constant temperatures ($T = 0$). In the laboratory, the upper boundary was in contact with air and was not kept at a perfectly constant temperature. We first subtract the hydrostatic pressure distribution and then introduce dimensionless variables using the scales defined above for temperature, length, velocity:

$$-\partial_z p + \frac{\nu_0}{\nu_1} \nabla^2 w_0 + \frac{g \alpha \Delta T R_\theta^2}{\nu_1 W_0} \theta = 0 \qquad z < h, \ z < 0, \qquad (9)$$

$$-\partial_z p + \frac{\nu_0}{\nu_1} \nabla^2 w_0 + \frac{g \alpha \Delta T R_\theta^2}{\nu_1 W_0} (\theta - B) = 0 \qquad 0 < z < h, \qquad (10)$$

$$-\partial_z p + \nabla^2 w_1 + \frac{g \alpha \Delta T R_\theta^2}{\nu_1 W_0} \theta = 0 \qquad z > h, \ z > 0, \qquad (11)$$

$$-\partial_z p + \nabla^2 w_1 + \frac{g \alpha \Delta T R_\theta^2}{\nu_1 W_0} (\theta + B) = 0 \qquad h < z < 0, \qquad (12)$$

$$\frac{D\theta}{Dt} - \frac{k \Delta T R_\theta}{Q} \nabla^2 \theta = 0 \qquad \forall z, \qquad (13)$$

where D stands for the total (material) derivative and p is the dimensionless dynamic pressure. The horizontal components of the momentum equation take a trivial dimensionless form and hence have been omitted. This system of equations depends on five dimensionless numbers: (1) $k \Delta T R_\theta / Q$, which provides a measure of the

Table 1. Parameters in the Experiments

Experiment	$\Delta \rho_c / \rho_0$	$\alpha \Delta T$	B	ν_1 / ν_0	ν_0, m s^{-2}
1	1.8×10^{-3}	1.2×10^{-3}	1.57	20	2.5×10^{-4}
2	1.7×10^{-3}	1.0×10^{-3}	1.71	28	2.5×10^{-4}
3	1.5×10^{-3}	1.0×10^{-3}	1.45	23	2.6×10^{-4}
4	1.4×10^{-3}	2.0×10^{-3}	0.71	22	2.8×10^{-4}
5	1.5×10^{-3}	2.0×10^{-3}	0.75	19	3.5×10^{-4}
6	1.5×10^{-3}	9.5×10^{-4}	1.54	22	3.0×10^{-4}
7	1.5×10^{-3}	1.4×10^{-3}	1.06	20	3.0×10^{-4}
8	1.8×10^{-3}	9.2×10^{-4}	2.01	10	3.0×10^{-4}
9	3.1×10^{-3}	9.4×10^{-4}	3.35	2.4	2.5×10^{-4}
10	1.6×10^{-3}	1.4×10^{-3}	1.17	18	3.0×10^{-4}
11	4.9×10^{-4}	1.4×10^{-3}	0.34	13	3.0×10^{-4}
12	5.6×10^{-4}	1.1×10^{-3}	0.49	18	2.8×10^{-4}
13	3.6×10^{-4}	1.5×10^{-3}	0.24	16	3.0×10^{-4}
14	5.0×10^{-4}	1.4×10^{-3}	0.36	15	3.1×10^{-4}
15	6.2×10^{-4}	1.1×10^{-3}	0.55	4.0	5.0×10^{-3}
16	6.8×10^{-4}	8.5×10^{-4}	0.80	4.0	5.0×10^{-3}
17	5.4×10^{-4}	1.4×10^{-3}	0.40	4.3	4.9×10^{-3}
18	4.9×10^{-4}	8.3×10^{-4}	0.59	16	3.3×10^{-4}
19	4.9×10^{-4}	8.6×10^{-4}	0.58	16	3.3×10^{-4}
20	2.7×10^{-3}	1.3×10^{-3}	2.08	5.4	2.6×10^{-4}
21	3.9×10^{-4}	2.0×10^{-3}	0.19	20	2.5×10^{-4}
22	3.6×10^{-4}	1.2×10^{-3}	0.28	16	3.2×10^{-4}

importance of diffusion in the heat equation (the inverse of a Peclet number), (2) $Ra = g \alpha \Delta T R_\theta^2 / \nu_1 W_0 = \rho_0 C_p g \alpha \Delta T^2 R_\theta^4 / Q \nu_1$, which provides a measure of the importance of buoyancy forces (a Rayleigh number), (3) B, the buoyancy ratio, (4) ν_0 / ν_1, the viscosity ratio between the layers, and (5) h_1 / R_θ, where the last dimensionless number, h_1 / R_θ, appears in the boundary conditions at the top of the upper layer.

[15] The characteristics of laboratory experiments and numerical simulations are listed in Tables 1 and 2. We have focused on two parameters which are likely to vary by large amounts in nature, the buoyancy ratio B and the viscosity ratio ν_1 / ν_0. Values for h_1 / R_θ are large, but, as explained above, the total width of the thermal anomaly is much larger than the scale length R_θ.

3. General Description

3.1. Different Phases of Interface Deformation

[16] Plume ascent through the lower liquid layer is uneventful and has been studied extensively. Figure 3 shows a plume at early times, before it impinges on the upper layer. The plume has developed a large head which, in this case, is about twice as large as the conduit. As discussed in Appendix C, temperatures in the plume head tend to be larger than in the conduit. This is due to the initial phase of heating before the beginning of plume ascent, which generates a large volume of hot fluid at the source. As shown by *Kaminski and Jaupart* [2003], the plume head is fed from below by heated fluid from the conduit and enlarges by diffusion. As the plume rises, therefore, the thermal anomaly in the head decreases progressively. For our experiments, the distance between the source and the upper layer is rather small, which probably implies that the magnitude of the plume head thermal anomaly is overestimated. Our experiments and calculations show that plume penetration proceeds over times that are large compared to the "incubation" time for the plume at the source. In such conditions, both the heat and mass budgets are dominated by the flux of material through the conduit.

Table 2. Parameters in the Numerical Simulations

Calculation	$\Delta\rho_c/\rho_0$	$\alpha\Delta T$	B	ν_1/ν_0	ν_0, m^2 s^{-1}
1	5.0×10^{-4}	6.4×10^{-4}	0.78	50	1.0×10^{-3}
2	5.0×10^{-4}	6.4×10^{-4}	0.78	100	1.0×10^{-3}
3	5.0×10^{-4}	6.4×10^{-4}	0.78	300	1.0×10^{-3}
4	5.0×10^{-4}	6.4×10^{-4}	0.78	700	1.0×10^{-3}
5	5.0×10^{-4}	6.4×10^{-4}	0.78	1000	1.0×10^{-3}
6	5.0×10^{-4}	4.2×10^{-4}	1.20	1	1.0×10^{-3}
7	5.0×10^{-4}	4.2×10^{-4}	1.20	10	1.0×10^{-3}
8	5.0×10^{-4}	4.2×10^{-4}	1.20	50	1.0×10^{-3}
9	5.0×10^{-4}	4.2×10^{-4}	1.20	100	1.0×10^{-3}
10	5.0×10^{-4}	4.2×10^{-4}	1.20	300	1.0×10^{-3}
11	5.0×10^{-4}	4.2×10^{-4}	1.20	700	1.0×10^{-3}
12	5.0×10^{-4}	4.2×10^{-4}	1.20	1000	1.0×10^{-3}
13	5.0×10^{-4}	2.2×10^{-4}	2.23	100	1.0×10^{-3}
14	5.0×10^{-4}	3.2×10^{-4}	1.55	100	1.0×10^{-3}
15	5.0×10^{-4}	4.2×10^{-4}	1.20	100	1.0×10^{-3}
16	5.0×10^{-4}	5.7×10^{-4}	0.88	100	1.0×10^{-3}
17	5.0×10^{-4}	6.4×10^{-4}	0.78	100	1.0×10^{-3}
18	5.0×10^{-4}	7.5×10^{-4}	0.67	100	1.0×10^{-3}
19	5.0×10^{-4}	4.2×10^{-4}	1.20	50	1.0×10^{-3}
20	2.5×10^{-4}	4.2×10^{-4}	0.60	50	1.0×10^{-3}
21	2.0×10^{-4}	4.2×10^{-4}	0.48	50	1.0×10^{-3}
22	1.5×10^{-4}	4.2×10^{-4}	0.36	50	1.0×10^{-3}
23	1.0×10^{-4}	4.2×10^{-4}	0.24	50	1.0×10^{-3}
24	2.0×10^{-3}	4.2×10^{-4}	4.80	100	1.0×10^{-3}
25	1.0×10^{-3}	4.2×10^{-4}	2.40	100	1.0×10^{-3}
26	7.5×10^{-4}	4.2×10^{-4}	1.80	100	1.0×10^{-3}
27	5.0×10^{-4}	4.2×10^{-4}	1.20	100	1.0×10^{-3}
28	3.5×10^{-4}	4.2×10^{-4}	0.84	100	1.0×10^{-3}
29	2.5×10^{-4}	4.2×10^{-4}	0.60	100	1.0×10^{-3}
30	1.0×10^{-4}	4.2×10^{-4}	0.24	100	1.0×10^{-3}
31	5.0×10^{-4}	4.2×10^{-4}	1.20	100	1.0×10^{-3}
32	5.0×10^{-4}	3.6×10^{-4}	1.41	100	1.0×10^{-3}
33	5.0×10^{-4}	3.1×10^{-4}	1.61	100	1.0×10^{-3}
34	5.0×10^{-4}	2.6×10^{-4}	1.96	100	1.0×10^{-3}
35	1.5×10^{-3}	1.5×10^{-3}	0.94	20	3.0×10^{-4}
36	1.6×10^{-3}	1.5×10^{-3}	1.03	18	3.0×10^{-4}
37	5.6×10^{-4}	1.2×10^{-3}	0.43	17	3.0×10^{-4}
38	4.9×10^{-4}	9.0×10^{-4}	0.52	17	3.0×10^{-4}
39	4.9×10^{-4}	9.3×10^{-4}	0.50	16	3.3×10^{-4}
40	2.7×10^{-3}	1.3×10^{-3}	1.96	5	3.0×10^{-4}

Experiment n°18

Figure 4. Plume penetration as a function of time for experiment 18, with $B = 0.59$ and $\nu_1/\nu_0 = 16$. The intrusion is bell shaped at $t = 10$, 15, and 25 min. At $t = 40$ min, the interface develops a cusp shape due to convective upwelling of the upper layer.

values of B, thermal buoyancy is small and cannot overcome the chemical density contrast and the plume essentially ponds beneath the upper layer. In experiment 20 with $B = 2.1$, for example, displacement of the interface is barely detectable. For smaller values of B, interface deformation is significant (Figures 4 and 5). Plume material loses heat to the upper layer, which develops thermal boundary layers above the deformed interface. This generates horizontal density differences, which are unconditionally unstable. Convective instability of the upper liquid was observed for all B values, inducing marked changes in the shape of

[17] The plume spreads laterally below the upper liquid and deforms the interface. Interface deformation is axisymmetric for all cases studied. The amount of vertical deformation is sensitive to the value of buoyancy ratio B. At high
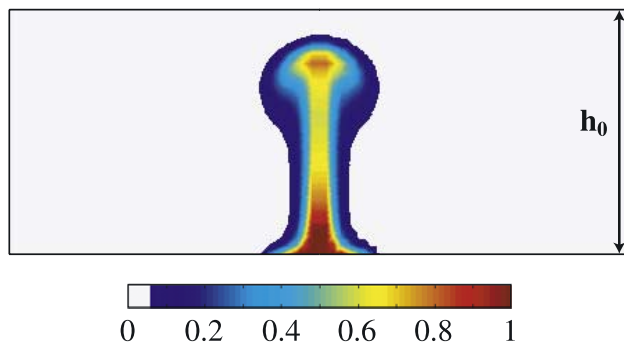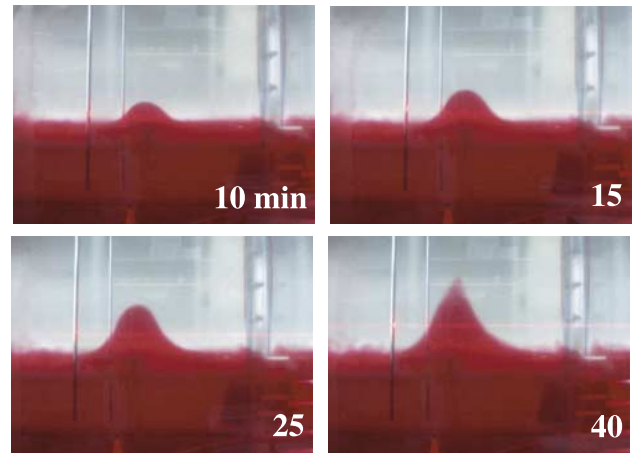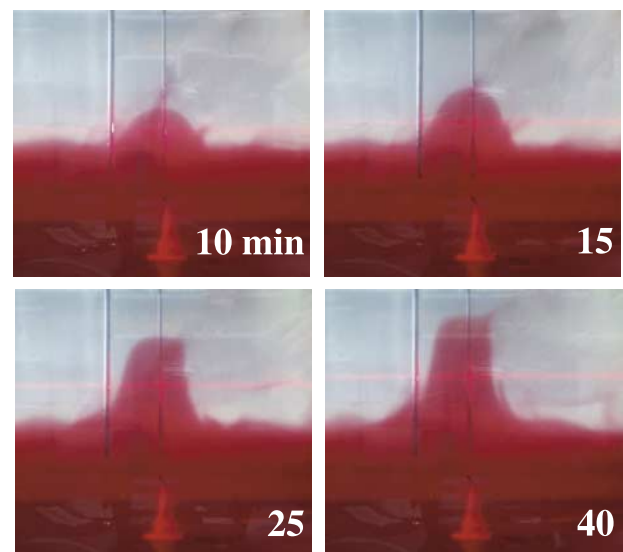

0   0.2   0.4   0.6   0.8   1

Figure 3. Temperature field in numerical simulation 19 with $B = 1.2$ and $\nu_1/\nu_0 = 50$ at early time, before the plume impinges on the upper layer. Scale is provided by the lower layer thickness h_0. The plume head is approximatively twice as large as the conduit. Note that it is at a higher temperature than the conduit just below.

Experiment N°12

Figure 5. Plume penetration as a function of time for experiment 12 with $B = 0.49$ and $\nu_1/\nu_0 = 18$. At this small B value, the plume penetrates to shallow levels and develops into a tall cylinder.
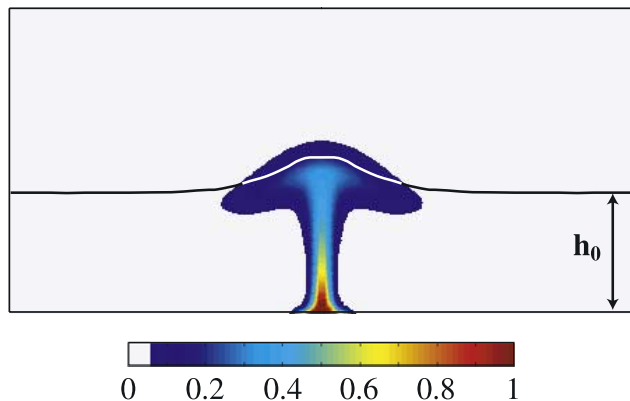
Figure 6. Temperature field in numerical simulation 19 with $B = 1.2$ and $\nu_1/\nu_0 = 50$. Both fluid layers are shown with their respective thicknesses. The interface is shown as the solid black and white line. Note that the plume material has spread over a large horizontal distance and that the upper layer has been heated over a significant thickness. A comparison with Figure 3, which shows the same case at an earlier time, shows that the plume head temperature anomaly has disappeared. Two effects are involved: the plume head has already passed and lost heat to the upper layer and the plume has risen to a larger distance above source.

the interface. An instability of similar characteristics, but different origin, has been documented by *Huismans et al.* [2001] in their study of lithosphere extension. We now describe in more detail experiments and calculations for two different values of B.

[18] For $B = 1.2$, the plume deforms the interface as it spreads horizontally (Figure 6). Interface deformation remains limited in the vertical direction and affects an increasingly larger area as time proceeds. With time, however, the upper layer becomes convectively unstable and the interface distorts into a cusp-like shape with a pointed top. Laboratory experiments and numerical calculations for the same parameter values lead to the same time

sequence and to interface shapes and dimensions that are almost identical (Figure 7).

[19] For B values less than about 0.6, flow eventually develops a strong vertical component and generates a tall intrusion with steep flanks. This marks the difference between interface deformation due to the ponding of buoyant material and true plume penetration. Figure 8 compares experiments and numerical calculations at low B ($\sim$0.49). In this case, the plume penetrates deeply into the upper layer. Eventually, as the plume rises to shallow levels, it starts spreading horizontally and develops an "anvil-shaped" cap. The upper layer also becomes unstable, but in this case it is due to heating at the quasi-vertical edges of the intrusion.

3.2. Dimensions and Shape of Interface Deformation

[20] Plume penetration is best tracked by monitoring the axial height of the interface as a function of time (Figure 1). Figure 9 shows data and numerical predictions for the moderate B case already illustrated by Figure 7 ($B \approx 1.2$, experiment 10 and calculation 36, Tables 1 and 2). For small times, after a brief initial acceleration period, the interface displacement is, within error, proportional to time, such that it proceeds at an almost constant velocity. The rate of vertical displacement slows down and then picks up dramatically as the upper layer becomes unstable. Note that in the first phase before the onset of convection, laboratory experiments and numerical calculations are in very good agreement. In the second phase after the onset of convection, the numerical calculations show a very small thread of lower liquid rising along the axis, entrained by the upwelling current set up in the upper liquid. This is picked up by the automatic procedure which locates the highest point reached by lower layer liquid. The thin axial thread is hardly detectable in the laboratory experiment and the visualization technique picks up the top of the "cusp" shaped intrusion. The two methods therefore track two different markers: the top of the bulk intrusion in the laboratory data, the tip of the axial thread in the numerical calculations. Figure 7 shows that the numerical calculation does a good job reproducing the intrusion dimensions and shape.
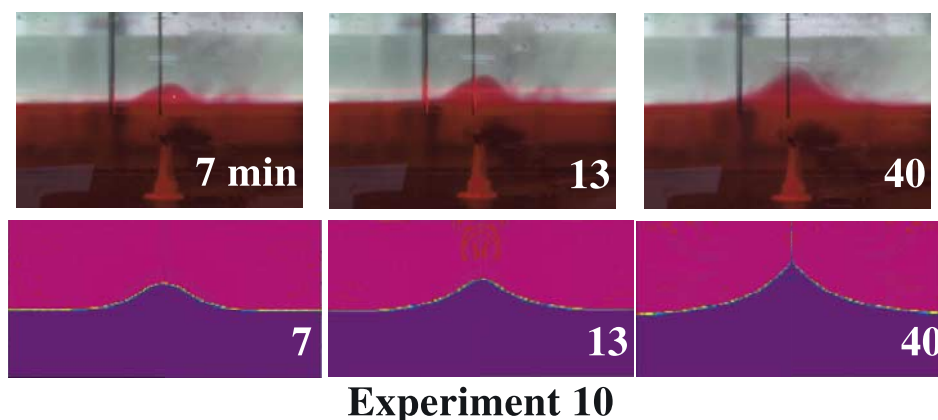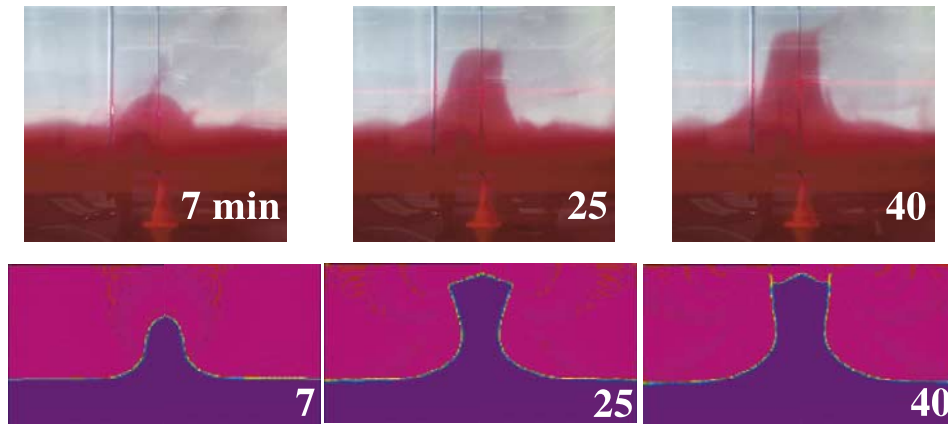

Experiment 10

Figure 7. (top) Experiment 10 at $B \approx 1.2$ and $\nu_1/\nu_0 = 18$. (bottom) Numerical analogue (simulation 36). Plots are drawn on the same scale, allowing direct comparison between the two. One may see that the numerical calculation reproduces the dimensions of the intrusion quite well. At $t = 40$ min, the upper layer has developed an active convective upwelling, and the intrusion has been distorted into a cusp. The numerical calculation has a slightly sharper cusp.

Experiment 12

Figure 8. (top) Evolution of the intrusion in experiment 12 at $B \approx 0.49$ and $\nu_1/\nu_0 = 18$. (bottom) Same evolution for its numerical analogue (simulation 37). Plots are drawn on the same scale. Convection in the upper layer distorts the interface into the shape of an anvil.

[21] Entrainment of lower liquid into the upper liquid is inevitable in the absence of surface tension and was observed in the laboratory experiments. With the numerical grid used here, such entrainment, materialized by thin threads rising above the cusp-shaped intrusion, is probably not well resolved. Thin threads are confirmed by calculations at higher resolution. They rarely spread over more than one grid spacing, however, and we did not attempt a quantitative analysis.

[22] To better describe the penetration sequence and changes of interface shape, we have determined two geometrical parameters. To calculate an aspect ratio, we determine the average radius R_{eq} corresponding to the equivalent cylinder with the same height and the same volume:

$$V = \int_0^h \pi R^2(z) dz = \pi R_{eq}^2 h. \tag{14}$$

To quantify the intrusion shape, we determine two half widths at $z/h = 3/4$ and $z/h = 1/2$. The ratio between the two, $R_{3/4}/R_{1/2}$, provides a good measure of shape: it is equal to 1 for a cylinder, ~ 0.64 for a Gaussian bell, 0.5 for a triangle and finally 0.24 for two circular quadrants back to back. For the cusp shapes due to induced convection, the shape ratio may even drop to values smaller than 0.24, showing that the interface may become very pointed indeed.

[23] Using these two geometrical indices, we monitor changes of intrusion shape as a function of time. Figure 10 shows how the shape ratio decreases with time in an experiment with $B = 1.2$. In a first phase, the interface gets deformed over a progressively larger horizontal extent and settles toward a Gaussian form with a shape ratio ≈ 0.64. A marked change occurs after convection has set in the upper layer, with the shape ratio tending to small values indicative of a cusp-shaped interface. The onset of convection occurs before the change of shape becomes marked and may be defined precisely using the velocity field. A detailed analysis of this is postponed to a companion study. In this experiment at a moderate B value, the interface does not deform to large heights in the upper layer and flow is weakly affected by the upper boundary.

[24] Values for the aspect ratio and the shape ratio are shown for all simulations at moderate or low B values (<2) in Figure 11. These determinations were all made at the end of the first phase, just before the onset of convection in the upper layer. Thus they correspond to different absolute times depending on the viscosities involved. At values of the aspect ratio less than about 1, all intrusions conform to a bell shape, and one should note the remarkable constancy of the shape ratio around a value of 0.6. For aspect ratios larger than about 1.3, the shape ratio is larger than 1, indicative of
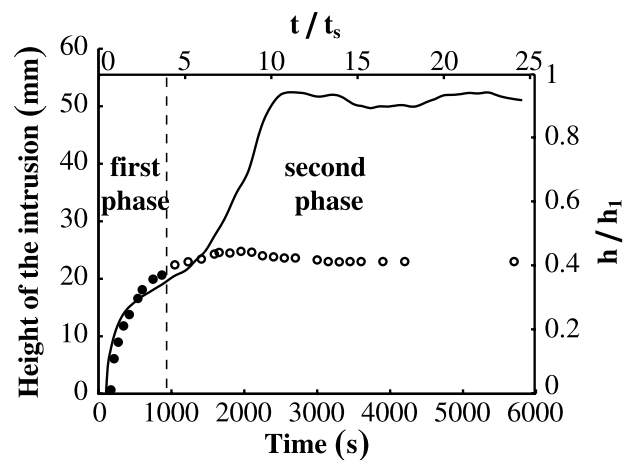

Figure 9. Height of the intrusion in experiment 10 (dots) and simulation 36 (solid line) which are made in almost identical conditions. In a first penetration phase, there is no convection in the upper layer. In the second phase, an active upwelling develops in the upper layer and entrains a thin thread of lower liquid which rapidly rises to shallow levels and almost reaches the top surface (horizontal line at $h/h_1 = 1$). The inflection point on the solid line marks the separation between the two phases. The laboratory technique tracks the top of the bulk intrusion and does not pick up the thin thread. Note the good agreement between the observed and calculated displacement values in the first deformation phase.
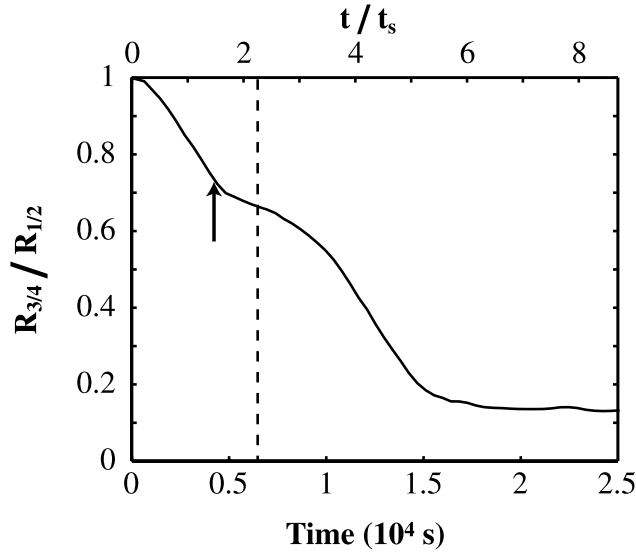
Figure 10. Shape ratio $R_{3/4}/R_{1/2}$ versus time for simulation 19 ($B = 1.2$). The shape ratio is approximately 0.6 for a Gaussian bell-shaped intrusion and drops to values less than 0.5 for a cusp. The dashed line separates the two different phases of interface deformation at the inflection point. The onset of convection in the upper layer occurs earlier at the time indicated by the arrow.

the vertical cylindrical shape which develops at small values of B. This is illustrated further by Figure 12, where the shape ratio for these experiments is plotted as a function of h/h_1. As B is larger than about 0.6, interface deformation extends over less than half the upper layer, the shape ratio takes "Gaussian" values. For B less than about 0.6, the plume is able to penetrate to shallow levels, such that h/h_1 is larger than 0.5, and the shape ratio takes large values. These results show that the displacement and shape of the interface are sensitive to the B value. From these, one may distinguish between two different behaviors: interface deformation for $B > 0.6$ and true plume penetration for $B \le 0.6$.

4. Scaling Analysis

[25] Convective instability of the upper layer due to heating by the plume is an important process which will be studied in detail in another paper. Here, we focus on what happens in the first phase of interface deformation, before the onset of convection in the upper layer. One goal is to show that one may indeed characterize deformation using only the plume characteristics at the interface, independently of distance from the source. A second goal is to derive scaling laws for interface deformation, which will be useful in the geological discussion. We focus on the axial interface height h. How the width of the deformed zone evolves can be deduced from the values of the aspect ratio and the shape ratio.

[26] All dimensionless variables can be written as functions of the five dimensionless numbers defined above. Therefore the axial intrusion height $h(t)$ is such that

$$\frac{h(t)}{R_\theta} = \mathcal{F}_o\left(\frac{t}{\tau}, \frac{k\Delta TR_\theta}{Q}, \frac{h_1}{R_\theta}, \frac{\rho_0 C_p g \alpha \Delta T^2 R_\theta^4}{Q\nu_1}, \frac{\nu_0}{\nu_1}, B\right). \quad (15)$$

4.1. Initial Interface Displacement Rate

[27] At small times, when the interface deformation is small, there is no convection in the upper layer but the physics of early plume interaction do not lend themselves to many simplifications. The shape of the interface changes markedly (Figure 10), implying that the flow field is not self-similar at all times. Further, the sharp temperature variations across the plume and the change of temperature distribution as the plume starts to spread induce a complex distribution of buoyancy forces. We search for a simple scaling relying on the following simplifications:

[28] 1. Thermal diffusion has little impact on the initial deformation. For small times, heat exchange between plume material and surrounding liquid affects small volumes and hence cannot modify significantly the total buoyancy force driving flow. This is expressed as $\rho_0 C_p \kappa \Delta TR_\theta/Q \ll 1$, implying that dimensionless function $\mathcal{F}_o$ can be taken in the limit of this number going to zero.

[29] 2. The upper boundary affects early plume ascent only weakly. As show by Figures 6 and 11, buoyancy forces are largest near the axis and the aspect ratio of interface deformation is of order 1. Thus, for early stages such that vertical displacements are small, the interface gets deformed over a lateral distance which is much smaller than h_1. In the
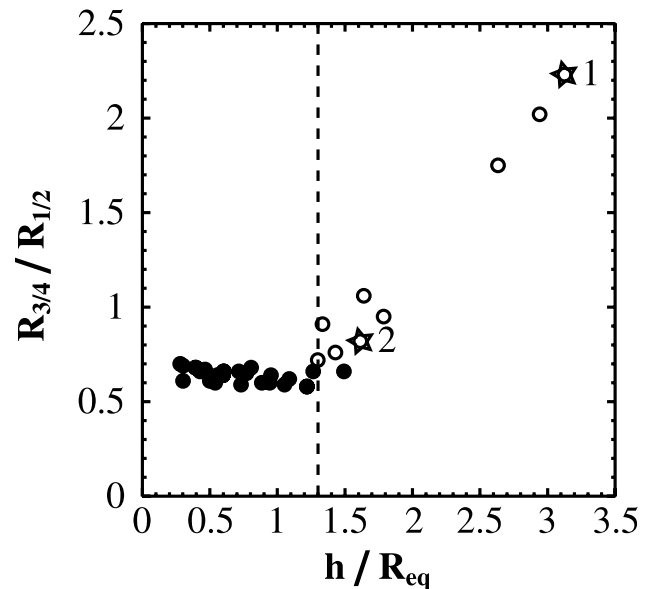

Figure 11. Shape of the interface at the end of the first deformation phase, just before the onset of convection in the upper layer, as a function of aspect ratio. Solid circles are $B > 0.6$; open circles and stars are $B < 0.6$. The data correspond to different physical times depending on the viscosities involved. The two stars correspond to two simulations with the same B value of 0.50 and two different values of the viscosity contrast: 17 for star 1 and 50 for star 2. One may define two populations depending on the aspect ratio, which also correspond to different ranges for B and hence to the two plume regimes. For $B > 0.6$, the aspect ratio is smaller than about 1.3, and the interface takes the shape of a Gaussian bell with a shape ratio of about 0.6. For $B < 0.6$, the aspect ratio takes larger values corresponding to the tall intrusion that develops.
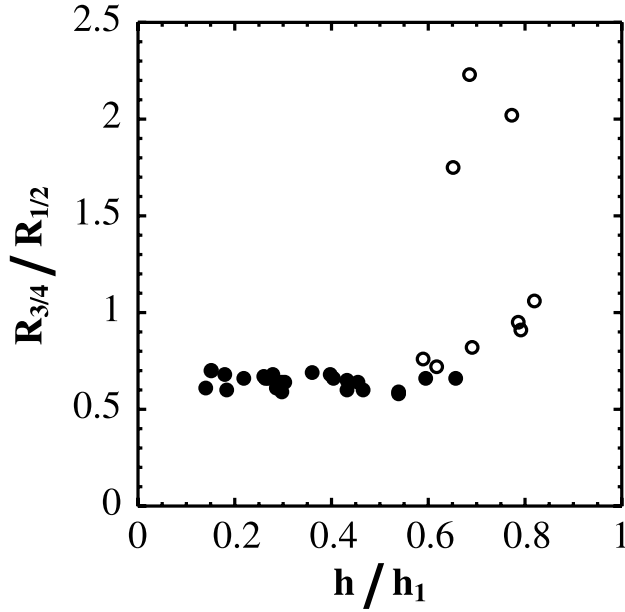
Figure 12. Shape ratio for the deformed interface, $R_{3/4}/R_{1/2}$, as a function of dimensionless interface height h/h_1. Solid symbols are $B > 0.6$. Open symbols are $B < 0.6$. In the interface deformation mode ($B > 0.6$), h/h_1 is less than 0.6, and the interface is deformed into a Gaussian bell. In the plume penetration mode ($B < 0.6$), h/h_1 takes larger values which typify the tall intrusion that develops.

upper layer, the flow field develops over a depth which scales with the width of the deformed zone, and hence over a depth which is also smaller than h_1. At small times, therefore, we expect that interface deformation is not sensitive to h_1 and that dimensionless function $\mathcal{F}_o$ does not depend on R_θ/h_1. In this analysis, "small times" are such that $h/h_1 \ll 1$, a condition that can be turned into one on time using the velocity scale which is obtained below.

[30] We thus assume that

$$\frac{h(t)}{R_\theta} \approx \mathcal{F}_o\left(\frac{t}{\tau}, \frac{\rho_0 C_p g\alpha\Delta T^2 R_\theta^4}{Q\nu_1}, \frac{\nu_0}{\nu_1}, B\right). \quad (16)$$

We further remark that the governing equations are not homogenous in parameter B, which can be corrected by rescaling temperature with B. This indicates that dimensionless number Ra must appear in combination with B. B also appears in the boundary condition for the plume temperature at the base of the lithosphere. The dimensionless variables (numbers) appearing in $\mathcal{F}_o$ are independent from one another and one may assume that they can be separated. For early times, one may expect a power law time dependence for height h and one may also assume that the dimensionless numbers appear through power laws:

$$h(t) = R_\theta\left(\frac{\rho_0 C_p g\alpha\Delta T^2 R_\theta^4 B}{Q\nu_1}\right)^m \left(\frac{tQ}{\rho C_p \Delta T R_\theta^3}\right)^n \left(\frac{\nu_0}{\nu_1}\right)^\beta \mathcal{G}(B). \quad (17)$$

[31] For small viscosity ratios close to 1 and for small values of the buoyancy number B, the upper layer is not

significantly different from the lower layer and the plume will go through the interface with little perturbation. This case is not relevant for our geological problem. For viscosity ratios that are significantly larger than 1, or for buoyancy numbers that are not small, the plume spreads laterally at the interface. This implies that the initial plume radius R_θ is not an important control variable for plume penetration. Thus one has $1 + 4m - 3n = 0$. Plume penetration in the upper, buoyant, layer involves an effective buoyancy flux, which is a function of buoyancy ratio B, and should not depend on explicitly on temperature scale ΔT. Thus one can write $2m - n = 0$. Using these two relations, we find $m = \frac{1}{2}$, $n = 1$, and hence

$$h(t) = \left(\frac{g\alpha QB}{\rho_0 C_p \nu_1}\right)^{\frac{1}{2}} \left(\frac{\nu_0}{\nu_1}\right)^\beta \mathcal{H}(B) \quad t, \quad (18)$$

where we recognize the velocity scale for a thermal plume with energy flux Q rising through fluid with viscosity μ_1:

$$W_1 = \left(\frac{g\alpha Q}{\rho_0 C_p \nu_1}\right)^{\frac{1}{2}}. \quad (19)$$

This relationship predicts an early phase of constant displacement rate, which is consistent with the experimental data and with the numerical results, as noted above. To determine the value of exponent β and function $\mathcal{H}(B)$, we have determined the initial displacement rate $[dh/dt]_0$ and consider the dimensionless ratio:

$$\frac{[dh/dt]_0}{\left(\frac{g\alpha QB}{\rho_0 C_p \nu_1}\right)^{\frac{1}{2}}} = \frac{[dh/dt]_0}{W_r} = \left(\frac{\nu_0}{\nu_1}\right)^\beta \mathcal{H}(B). \quad (20)$$

Keeping B constant, we determine that exponent $\beta \approx \frac{1}{4}$ (Figure 13). Using that result, we next find that $\mathcal{H}(B) \approx 0.4/B$ for all our calculations (Figure 14). To summarize, we obtain

$$h = 0.4 \quad \left(\frac{g\alpha Q}{\rho_0 C_p \nu_1 B}\right)^{\frac{1}{2}} \left(\frac{\nu_0}{\nu_1}\right)^{\frac{1}{4}} \quad t, \quad (21)$$

which is only valid for small times. Note that the displacement rate decreases with B, as may be expected. This analysis shows that plume penetration depends only on the local plume characteristics at the interface, independently of distance from source.

4.2. Final Plume Penetration

[32] We also seek controls on the height reached by the plume. In the experiments and the calculations, true steady state is only achieved after the onset of convection in the upper layer (Figure 9), but the onset time provides a convenient reference.

[33] For $B > 0.6$, in the deformation mode, the interface gets displaced over large horizontal distances. In this case, velocities are dominantly horizontal in the lower liquid and negligible in the upper fluid. In these conditions, the vertical momentum balance reduces to a hydrostatic balance. At steady state, a constant temperature gradient is maintained through the thinned upper layer and, by continuity, in a
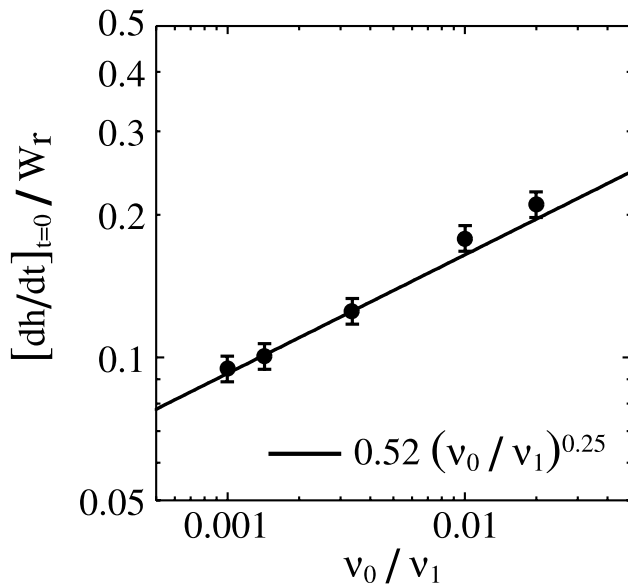
Figure 13. Initial rate of vertical deformation for 5 calculations with $B = 0.78$ as a function of viscosity contrast. The solid line has a slope of 1/4.

boundary layer at the top of the spreading plume material. Instead of solving for the steady state involving an advection-diffusion balance, we approximate the vertical temperature profile by a constant gradient extending over h_1, through both the lower liqui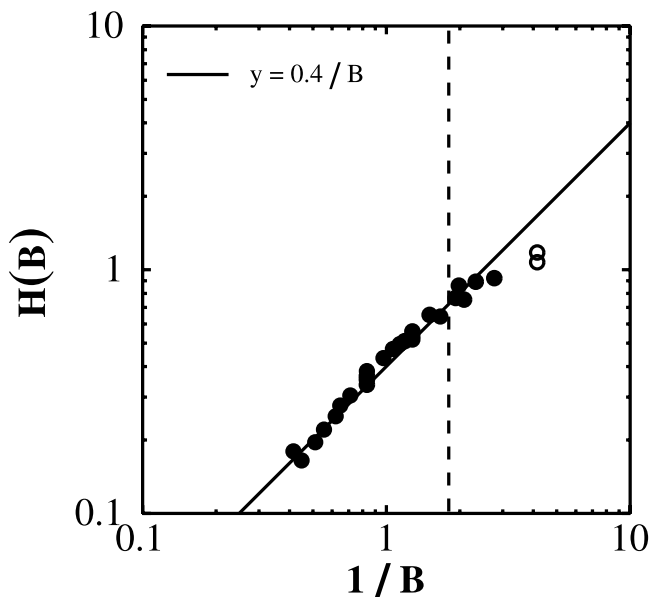d up to $z = h$ and the upper liquid for $h < z < h_1$. As shown in Figure 15, calculated vertical temperature profiles along the axis at two different times approach this simple linear profile.

[34] The isostatic balance yields

$$\frac{h_{iso}}{h_1} = \frac{1}{2B}. \qquad (22)$$

This relationship is only valid for $B > 1/2$, which is consistent with the starting assumption of $B > 0.6$. This result relies on an idealized thermal structure, but one may show that it takes large deviations from this idealization to introduce significant differences.

[35] The key feature is that plume material loses heat to the upper layer, in contrast to the case of a purely chemical plume. Heating the upper liquid eventually drives a local instability, which changes the physics of interface deformation. Here, we restrict ourselves to the first phase of deformation, before the onset of convection. We have determined the axial interface position at the end of this first phase, noted h_f, in our numerical calculations and plot it as a function of B in Figure 16. In some cases, at the largest values of the viscosity contrast and for the smallest plume energy fluxes, instability of the upper layer took very large times and calculations had to be terminated before. We obtained very similar results with the laboratory experiments but do not show them on the same figure because the onset of instability cannot be determined with the same accuracy. One may see that the approximate thermal structure illustrated in Figure 15 provides an upper bound on h_f and that interface height scales roughly with $h_s = h_1/B$ (Figure 16). One interesting feature is that the data follow different trends for $B > 0.6$ and $B < 0.6$, corresponding to the two different types of plume behavior. For practical
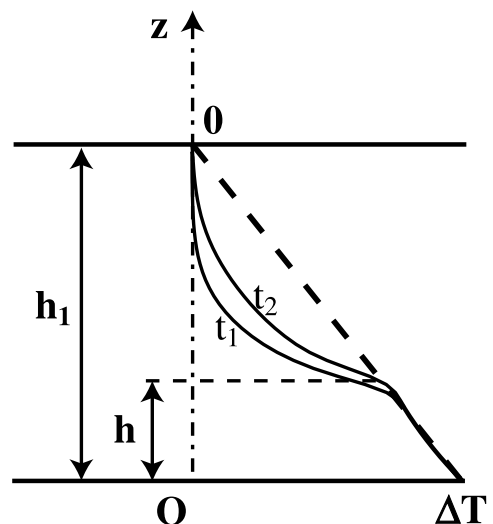

Figure 14. Dimensionless function $\mathcal{H}(B)$ for the initial rate of vertical deformation, as a function of B for all numerical calculations. Open symbols correspond to calculations 23 and 30 at very low values of B, such that plume penetration is very rapid and proceeds almost to the top of the upper layer. The vertical dashed line corresponds to $B = 0.6$, which separates the two different plume behaviors.

Figure 15. Vertical temperature profiles along the axis through both the lower liquid (up to $z = h$) and the upper liquid (for $h < z < h_1$) for calculation 19 at two successive times t_1 and t_2. These show that plume material loses heat to the overlying liquid. The marked change of curvature lies at the interface, which migrates upward from t_1 to t_2. The reference linear temperature profile is an approximation to the steady state profile which is used in an isostatic balance.
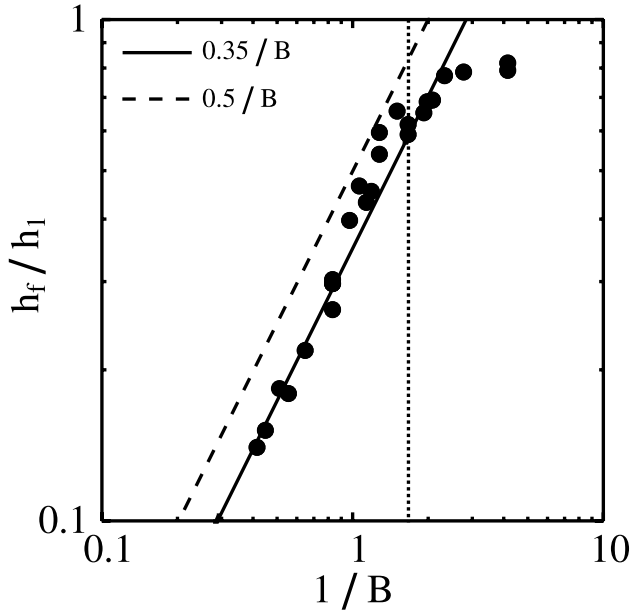
Figure 16. Dimensionless interface position h_f/h_1 at the end of the first deformation phase, before the onset of convection in the upper fluid, as a function of $1/B$. The dashed line corresponds to the fully developed linear temperature profile shown on Figure 15. The solid line corresponds to a best fit through the data points. The vertical dotted line corresponds to $B = 0.6$, which separates the two different plume regimes.

purposes, it is sufficient to approximate final plume heights using the best fit relationship:

$$h_f = 0.35 \, \frac{h_1}{B}. \tag{23}$$

Departures from this relationship never exceed ±20%, which is sufficiently precise for geological applications given the uncertainties that affect most variables and properties. Of course, the full numerical solution can be used if need be. For $B < 0.6$, the plume penetrates with a large vertical velocity component and the preceding analysis is no longer valid. For such small buoyancy numbers, the plume is expected to reach the top of the upper layer.

4.3. Time Dependence of Plume Penetration

[36] Past the initial phase which is not sensitive to thermal diffusion and to the presence of the upper boundary, we have found no universal scaling law to describe the interface deformation. The effects of thermal diffusion are important, as explained above, and develop over time. Depending on viscosity values, which determine the timescale of interface deformation, they affect the distribution of buoyancy forces in different ways. Collapsing results for B values larger and smaller than 0.6, which involve different interface behaviors, onto a single master function may in fact seem far fetched. We use $h_s = h_1/B$ as the relevant length scale and the initial deformation rate, W_s, as velocity scale:

$$W_s = \left(\frac{g\alpha Q}{\rho_0 C_p \nu_1 B}\right)^{\frac{1}{2}} \left(\frac{\nu_0}{\nu_1}\right)^{\frac{1}{4}}. \tag{24}$$

We deduce a new timescale:

$$t_s = \frac{h_s}{W_s} = \frac{h_1}{\left(\frac{g\alpha QB}{\rho_0 C_p \nu_1}\right)^{\frac{1}{2}}} \left(\frac{\nu_1}{\nu_0}\right)^{\frac{1}{4}} \tag{25}$$

and consider the relationship between dimensionless interface height h/h_s as a function of dimensionless time t/t_s. In order to evaluate the effects of the different variables, we have considered two sets of results with all parameters constant save one, one in which only B varies and the other in which only the viscosity ratio varies (Figures 17 and 18). By construction, the curves all collapse onto a single one at small times and remain close to one another. The scatter has already been documented in Figure 16 and reflects the imperfect model for the thermal structure. The results shown span almost 2 orders of magnitude in viscosity contrast and 1 order of magnitude in B values. For practical purposes, one may consider that plume penetration is complete at $t/t_s \approx 2$.

5. Discussion
5.1. Relevance of the Model to the Earth

[37] It is clear that the present model is not a perfect analog of the lithosphere-asthenosphere system. Listing all the complications that arise in nature and evaluating their influence on the results would not be very useful, and we focus on the key findings that are robust, i.e., that should not be affected by complications to the model setup. One is that mantle plumes may have two different behaviors depending on the values of buoyancy number B. The change of behavior occurs at $B \approx 0.6$, and not at $B \approx 1$ as a simple local neutral buoyancy argument (i.e., $\Delta\rho_T \approx \Delta\rho_c$) would suggest. This is due to the fact that plume material loses heat to the lithosphere, which acts to reduce its effective buoyancy. Another result is that the lithosphere thins even at B values larger than 1: plume material which ponds at the
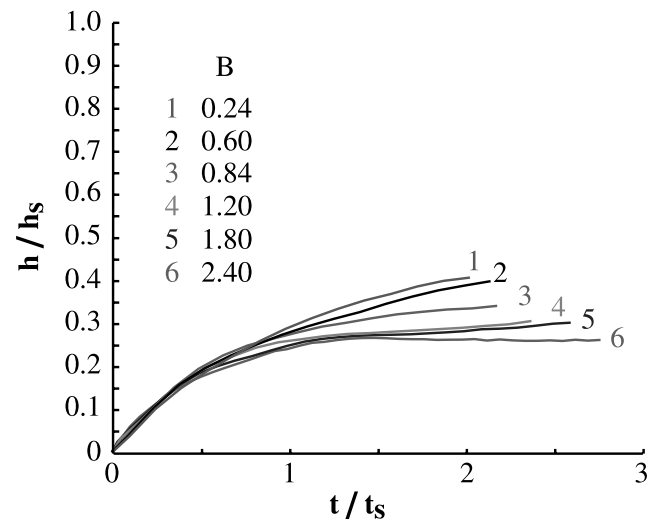

Figure 17. Dimensionless interface position h/h_s as a function of dimensionless time t/t_s for six calculations at different values of B with all other parameters kept constant ($\nu_1/\nu_0 = 100$).
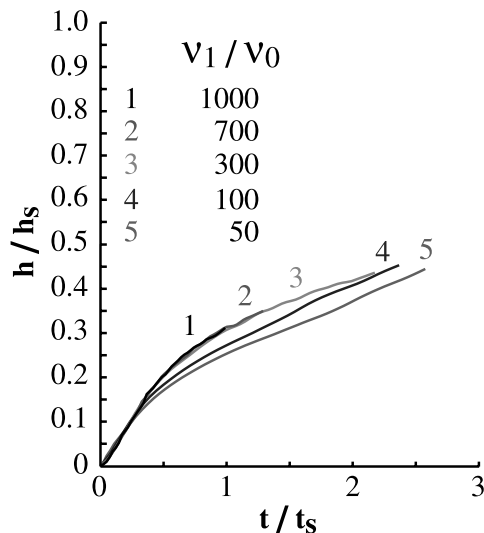
Figure 18. Dimensionless interface position as a function of dimensionless time t/t_s for five calculations at different values of viscosity ratio ν_1/ν_0 with all other parameters kept constant ($B = 0.78$).

base of the lithosphere applies an upward buoyancy force. A third result is that heated lithosphere probably becomes unstable, which generates a secondary upwelling above the plume itself.

[38] Temperature-dependent viscosity is not likely to affect plume behavior in the same manner for all values of B. For $B > 0.6$, the upper layer responds to the buoyancy force applied at its base such that the interface tends toward a position dictated by isostasy. The characteristic time will be a function of the overall viscosity structure. For $B < 0.6$, we may expect that plume penetration gets slowed down by the increasingly viscous surroundings. One may envision two competing effects. On the one hand, as the intrusion develops more slowly, the continuing plume supply generates a laterally more extensive heated region at the base of the upper layer, which tends to widen the intrusion. On the other hand, the focussing of heat flow at the plume axis acts to soften the upper layer there and to enhance localization of vertical motion, which tends to sharpen the intrusion. This question clearly deserves further study. At very large variations of viscosity, plume penetration should be entirely governed by thermal softening and hence by the efficiency of heat transfer between the plume and surrounding lithosphere. In a compositionally homogeneous lithosphere, the asymptotic depth of penetration is probably controlled by the rheological variations [*Moresi and Solomatov*, 1995; *Solomatov and Moresi*, 1997].

[39] In their study of thermal plumes in fluids with temperature-dependent viscosity, *Moore et al.* [1999] found that at large temperature contrasts and large activation energies, nonaxisymmetric instabilities develop within the plume. These instabilities enhance heat transport from hot plume material to the lithosphere and act to speed up plume penetration. We have observed these instabilities neither in the laboratory experiments, where they would show up as temperature fluctuations, nor in the numerical calculation, which allowed for nonaxisymmetric flows. *Moore et al.* [1999] observe two different kinds of instabilities, involving

vertical temperature gradients at the interface on the one hand and the moving front separating the plume and the lithosphere on the other hand. The former is caused by the growth of an unstable thermal boundary layer encompassing both plume material and the lithosphere (Figure 15). Two conditions must be met for instability: the local Rayleigh number for this boundary layer must exceed a critical value [*Parsons and McKenzie*, 1978] and the temperature difference across it must exceed the "rheological" temperature contrast [*Davaille and Jaupart*, 1994]. The latter condition does not apply to the present study. As regards the former one, there is a fundamental difference between the present study and that of *Moore et al.* [1999]. In the latter, the lithosphere is made of the same material as the asthenosphere and may take part in the instability. In our case, it is stabilized by its intrinsic buoyancy and viscosity contrast, implying that instability can only involve that part of the thermal boundary layer which lies below the interface. This sublayer is thinner than the full thermal boundary layer and the temperature difference across it is smaller than the total plume thermal anomaly ΔT. Both factors act to decrease the local Rayleigh number for the potentially unstable layer and hence to enhance stability. Small-scale instabilities are inevitable at large plume temperatures, but the threshold plume temperature must be higher than predicted by *Moore et al.* [1999]. This interesting topic deserves an independent investigation.

5.2. Geological Implications

[40] As explained at the beginning of this paper, typical values of plume temperature anomalies and intrinsic buoyancy of subcontinental lithospheric mantle are such that the buoyancy ratio B hovers around the critical value of 0.6. Therefore it should come as no surprise that lithosphere response to a plume is highly variable. This may also explain why there are two different kinds of continental flood basalts [*Turner et al.*, 1996]. As discussed below, one additional factor is the drift velocity of the lithosphere with respect to the plume. Combining plume energy flux, lithosphere buoyancy and drift velocity in various ways offer a wealth of different behaviors which can be analyzed systematically and quantitatively. This offers an interesting alternative to models involving passive stretching due to far-field tectonic forces whose magnitudes remain poorly known.

[41] As discussed in the introduction, the buoyancy ratio for Archean lithosphere can only decrease below the threshold value of 0.6 if an exceptionally strong mantle plume is involved. For typical present-day plume characteristics and the average density given by *Poudjom-Djomani et al.* [2001], the Archean B value is larger than 1, implying deformation over a small vertical extent and large horizontal distances. For Phanerozoic lithosphere, the buoyancy ratio may be as small as 0.5, implying much more extensive plume penetration. In this case, the resulting asthenospheric intrusion may be nearly vertical if the plume remains active for sufficiently long. Such an intrusion is a good candidate for the narrow lithospheric seismic anomaly beneath the south central Saskatchewan kimberlite field of Canada [*Bank et al.*, 1998]. For oceanic lithosphere, the intrinsic density is only slightly lower than that of the convective mantle, implying a small B value and hence extensive

vertical plume penetration. One crucial factor, however, is plate motion with respect to the plume source, which implies that a small length of time is available for plume penetration at any location. In this case, the extent of plume penetration depends on the ratio between the interface displacement rate, W_s, given above, and the "drift" velocity of the lithosphere with respect to the plume, W_{drift}. One may expect a range of behaviors as a function of ratio W_s/W_{drift}. At very small values of this ratio, interface deformation and plume penetration are negligible. Conversely, at very large values of this ratio, lithosphere motion does not affect plume behavior.

[42] We can estimate the velocity of plume penetration using the scaling laws derived above. For the sake of example, we take $B \approx 1$, $\mu_1 = 10^{21}$ Pa s, $\mu_1/\mu_0 = 10^2$ and $Q = 10^{11}$ W, corresponding to a plume of average strength [*Sleep*, 1990]. For these values, we find that the initial upward displacement rate is about 10^{-9} m s^{-1}, or 3 cm yr^{-1}. This estimate is close to, but smaller than, the drift velocity of the Pacific plate, for example. This indicates that this hypothetical thermal plume would be able to affect the Pacific plate significantly but that it would not be able to penetrate to the full extent predicted by the fixed configuration of the present work. It would take such a plume about 50 Ma to go through 100 km of lithosphere. The viscosity value for the lithosphere is not well constrained, which affects the reliability of this calculation. From our scalings, changing this viscosity by 1 order of magnitude leads to change the displacement rate by a factor of 5.

[43] A recent study of the Hawaiian hot spot track by *Li et al.* [2004] indicates significant thinning of the lithosphere. Thinning is small under Big Island, which lies directly above the Hawaiian plume today, and reaches $\approx$50 km beneath Kauai which was affected by the plume about 5 Myr ago. This allows an estimate of 1 cm yr^{-1} for the thinning rate above the Hawaiian plume. Because of lithosphere drift, this value is smaller than that for a static lithosphere.

[44] One important result of this investigation is the existence of two different phases of plume penetration and interface deformation, characterized by different upwelling velocities and interface shapes. The lithosphere-like layer, which is probably in a state of marginal stability [*Parsons and McKenzie*, 1978; *Cottrell et al.*, 2004], gets destabilized above the plume after some finite amount of time. The induced decompression and entrainment of material from the asthenosphere-like lower layer has interesting implications for melt genesis and composition which are not explored here due to space limitations.

6. Conclusion

[45] Comparison between laboratory experiments and numerical simulations demonstrate that the tracer method used to track deformation of the lithosphere-asthenosphere interface works well. Scaling analysis demonstrates that the characteristics of plume penetration depend only on the local plume characteristics, independently of distance to the source. The key parameter is the buoyancy ratio B which takes values close to 1 for Archean and Proterozoic continental lithospheres. The viscosity contrast determines the timescale of interface deformation, but has no effect on the

final amplitude and shape of the deformation. Plume behavior is easy to predict in the two limits of large and small values of B, but geological cases span the intermediate range where we observe marked differences of behavior. This implies that small differences of composition and intrinsic density can have large consequences on the manner of lithosphere deformation by a thermal plume. If $B \geq 2$, plume buoyancy is negligible and there can be no significant deformation. If $0.6 < B < 2$, plume material does not really penetrate into the upper layer and ponds beneath the interface. In this case, the interface deforms and gets displaced vertically, but the amount of vertical deformation is small compared to the amount of horizontal deformation. If $B < 0.6$, the vertical deformation component dominates, which we describe as "true" plume penetration into the upper layer. In this case, the plume generates a narrow and almost vertical intrusion.

[46] The experiments and calculations show that thermal diffusion is not important in early stages, but that it plays a key role in later stages. This is shown by the final penetration height and also by the fact that the lithosphere-like layer eventually becomes unstable. The combined effects of interface deformation and heat exchange between the two fluids induce a range of behaviors and a range of deformation characteristics. This implies that plumes have different effects on the lithosphere depending on the temperature anomaly and on the composition of lithospheric mantle.

Appendix A: Laboratory Experiments

A1. Apparatus and Working Fluids

[47] The experimental challenge was to produce a viscous buoyant layer on top of denser liquid with very small intrinsic density contrasts (typically less than 1%) and to avoid surface tension effects which are negligible on the scale of Earth's mantle processes. Working fluids are aqueous solutions of glycerol and cellulose (trade mark Natrosol). We use glycerol to set the density and cellulose to set the viscosity. Adding less than 2% Natrosol allows viscosity variation of up to 10^5 without affecting other physical properties. For the low deformation rates of convective phenomena, such solutions behave as incompressible Newtonian liquids [*Tait and Jaupart*, 1989, 1992]. With such miscible liquids, viscosity and density contrasts can be varied independently, and the Prandtl number takes large values: in the present set of experiments, it was always larger than 1800. The physical properties of the working solutions were measured in the laboratory for each experiment. Density is measured with an accuracy of $\pm 5 \ 10^{-6}$ g cm^{-1} using an oscillating U-tube density meter. Viscosity is measured with an accuracy of $\pm 15\%$ using a rotating viscometer. The viscosity of the glycerol-cellulose solution is a weak function of temperature:

$$\frac{\eta(T)}{\eta(20°C)} = 2.45 \ \exp(-0.045 \ T), \quad (A1)$$

with T in °C [*Lebars and Davaille*, 2004]. All the relevant physical properties are listed in Table A1.

[48] We used a 30^3 cm^3 Plexiglas tank with 3 cm thick walls which achieves very good thermal insulation (Figure 1). Mechanical boundary conditions are free slip

Table A1. Physical Properties of the Fluids

Properties	Water	Lower Layer	Upper Layer
μ, Pa s	$1\ 10^{-3}$	$0.25 \leq \mu_0 \leq 5$	$0.6 \leq \mu_1 \leq 21$
α, K^{-1}	2.2×10^{-4}	2.65×10^{-4}	2.65×10^{-4}
C_p, J K^{-1} kg^{-1}	4180	$\sim$4180	$\sim$4180
κ, m^2 s^{-1}	1.44×10^{-7}	1.44×10^{-7}	1.44×10^{-7}
σ	7	$1,800 \leq \sigma \leq 35,000$	$4,250 \leq \sigma \leq 150,000$
Density, 20°C	0.99820	$1.00048 \leq d \leq 1.00208$	$0.99909 \leq d \leq 1.00020$
Thickness		5 cm $\leq h_0 \leq$ 10.1 cm	5.2 cm $\leq h_1 \leq$ 19.3 cm
Power input, W		$1.39 \leq Q \leq 3.5$	

at the top and rigid everywhere else. A 4 mm diameter electrical coil is placed on a small plastic stand above the base of the tank and fed by a DC generator. Resistance and ohmic dissipation are continuously monitored through the experiment. The room is thermostated at 20°C. We worked with small values of power input, in a range of 1 to 5 W, which gives small temperature anomalies in the plumes (less than 10 K), so that the fluid physical properties vary by small amounts. The viscosity contrast between the plume axis and the far field was always less than 40%.

[49] Because of the very small density difference between the two liquids (Table A2), filling the tank without mixing is tricky. The solutions have two different additives and hence double-diffusive convection is bound to occur, driven by concentration gradients which build up at the interface [e.g., *Turner*, 1973, pp. 254–287]. In practice, we had about 3 hours before double-diffusive fingering was observed.

[50] Initially, both fluid layers are at room temperature, such that the vertical profiles of density and viscosity are step functions. At $t = 0$, a constant power is supplied at the base of the lower layer. Conditions and parameter values are listed in Table A2 for 22 experiments.

A2. Measurements

[51] Twenty-one thermocouples are used to measure temperature over two vertical profiles: one at the plume axis and another at a radial distance of 1 cm. Temperatures are determined to within ±0.025 K by a scanning voltmeter every 30 s. Thermocouples are encased in thin metal probes (2 mm and 3 mm diameter) which offer very small resistance to the flow. Their location is known to within ±0.2 mm.

[52] To keep track of plume penetration into the upper layer, we used a mobile laser system which was moved up and down in order to avoid parallax effects. Once the height of the plume was known, we moved the laser to half this height and took a photograph, which allowed determination of plume width (Figure A1). The top of the plume was located to within ±0.5 mm, due to the size of the laser beam. Plume width is measured to within ±2.5 mm because the color contrast is weaker at the edge of the plumes.

Appendix B: Numerical Model

[53] Comparison with the experiments involves two issues. One is that experiments are by definition carried

out for finite values of the Prandtl number whereas the calculations were made in the infinite Prandtl number limit appropriate for geological cases. Another issue is that calculations and experiments cannot be made with exactly the same heat source characteristics.

B1. Method

[54] Governing equations for convection need not be reproduced here. Salient features are that they are written in the Boussssinesq approximation and in the infinite Prandtl number limit, such that inertial terms and viscous dissipation are neglected in the momentum and energy equations. Fluids are incompressible and Newtonian with constant viscosity. Sidewalls are reflecting and, as in the laboratory, the base is rigid and the top is free slip. At the top of the domain, temperature is kept at a constant value. The base is thermally insulated except for a square patch where a constant and uniform heat flux is imposed.

[55] Calculations are made with the STAG3D program [*Tackley*, 1994, 1996], which uses a multigrid scheme to achieve rapid convergence. The program has been modified in order to generate the desired bottom boundary condition. The upper layer is represented by active tracers which are advected along the velocity field. The concentration of tracers in a cell allows tracking of composition and material properties. Density is a linear function of the tracer concen-
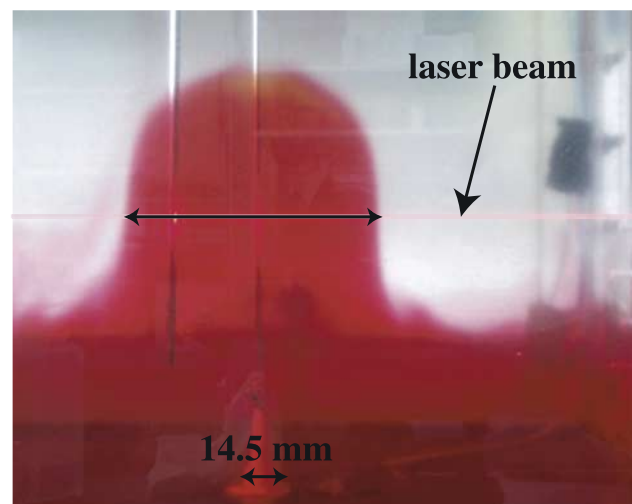

Figure A1. A well-deformed interface in experiment 17 with a horizontal laser beam which is used to determine the top of the interface and the width of the deformed region. The small heater used to generate a thermal plume in the lower liquid is seen at the bottom.

Table A2. Parameters in the Earth, in the Experiments, and in the Numerical Simulations

Parameters	Earth	Experiments	Calculations
ν_1/ν_0	>1	4–22	1–1000
$B = \Delta\rho_c/\Delta\rho_T$	$\sim$0.5–2	0.2–2.1	0.24–4.8

tration which ensures mass conservation. At $t = 0$, the compositional field varies from $C = 1$ in the upper layer to $C = 0$ in the lower layer. At each time step, the chemical field is calculated and used to determine the density and viscosity fields. The computational domain is set in Cartesian coordinates with $n_x \times n_y \times n_z$ cells. We solve for all variables in one quadrant ($x > 0$ and $y > 0$) so that we may detect nonaxisymmetric instabilities. All variables are symmetrical with respect to the vertical axis. The aspect ratio is 1 for the computational domain and 2 for the "physical" box. Most calculations are carried out with $n_x = n_y = n_z = 64$, and a few were made with $n_x = n_y = n_z = 128$ or 256 in order to assess the accuracy of the numerical results. The number of tracers per cell must be large enough to limit statistical noise [van Keken et al., 1997]. For $n_x = n_y = n_z = 64$, the use of 64 active tracers per cell is a good compromise between precision and calculation cost [Tackley and King, 2003]. Values for the input parameters and variables in the numerical simulations are listed in Table 2. Several calculations were designed to reproduce laboratory experiments.

B2. Outputs

[56] A post processing scheme using a second-order polynomial interpolation is performed to derive values for temperature and velocity at the plume axis. With a finite grid size, the position of the interface is not known with great accuracy, all the more as the interface looses its sharpness with time, with the tracer concentration increasing from 0 to 1 over more than one grid spacing. Going upward along vertical profiles of tracer concentration, we first get a rough estimate, noted $h_{ro}(x, y)$, such that the tracer concentration first increases above 0. Tracers are only advected and there is no chemical diffusion. Velocities are mainly vertical and mass conservation over a vertical column leads to a more accurate estimate of the interface position:

$$h_{ro}(x,y) + \int_{h_{ro}}^{h_{ro}+\Delta} [1 - C(x,y,z)] \, dz = h_1(x,y), \quad (B1)$$

where $C(x, y, z)$ is the tracer concentration and Δ is the vertical distance over which the tracer concentration varies from 0 to 1. With this method, the error on the interface position is less than one grid size.

Appendix C: Calibration

C1. Laminar Plumes: Theory and Experiments

[57] As shown by Batchelor [1954], scales for vertical velocity and temperature in a thermal plume rising through an unbounded isoviscous fluid are

$$W_B \propto \left(\frac{g\alpha Q}{2\pi\rho C_p \nu} \right)^{\frac{1}{2}} \quad (C1)$$

$$\Delta T_B(z) \propto \frac{Q}{\rho C_p \kappa z}. \quad (C2)$$

One consequence is that a thermal plume rises at a constant velocity [Fujii, 1963; Brand and Lahey, 1967].

According to the asymptotic analysis by Worster [1986], the centerline ascent velocity depends on the Prandtl number as follows:

$$W_W = \left(\log \epsilon^{-2} \right)^{\frac{1}{2}} \left(\frac{g\alpha Q}{2\pi\rho C_p \nu} \right)^{\frac{1}{2}}, \quad (C3)$$

where ϵ is the solution of

$$\epsilon^4 \log \epsilon^{-2} = \sigma^{-1} \quad (C4)$$

and the axial temperature anomaly at height z above the heat source is

$$\Delta T_W(z) = a(\sigma) \frac{Q}{2\pi\rho C_p \kappa z}, \quad (C5)$$

where $a(\sigma)$ is a function of the Prandtl number σ such that $\lim_{\sigma \to \infty} a(\sigma) = 0.5$.

C2. Plumes in the Laboratory

[58] Laboratory experiments have shown that starting plumes can be understood using the steady plume theory [Moses et al., 1993; Couliette and Loper, 1995; Kaminski and Jaupart, 2003]. The theory is only valid for plumes which extend over large vertical distances. One problem is that in this case, the momentum boundary layer also extends over large horizontal distances. For example, in a box of radius R_{box}, the largest Prandtl number for which wall effects can be neglected is [Kaminski and Jaupart, 2003]

$$\sigma_{\max} \approx \left(\frac{R_{box}^2 g\alpha Q}{\rho C_p \kappa^3} \right)^{\frac{1}{3}}. \quad (C6)$$

[59] For our high Prandtl number fluids ($\sigma \geq 2000$), a very good approximation for coefficient $a(\sigma)$ in equation (C5) is $a(\sigma) \approx 0.5$. In the experiments, power is generated by ohmic dissipation in a small electrical coil. In steady state, the coil and its small stand are maintained at an elevated temperature and hence some heat is diverted to the tank base. We introduce the power leakage Q_o such that the true plume energy flux is $Q - Q_o$. The source has finite dimensions and plume characteristics conform to the point source model only at large distance. One may introduce a virtual point source located at distance z_0 beneath the true source such that the virtual plume has the same characteristics than the true one (Figure 2). The axial plume temperature at height z above source is

$$\Delta T(z) = C_e \frac{1}{2\pi\rho C_p \kappa} \frac{Q - Q_0}{z - z_0}, \quad (C7)$$

where C_e is a numerical constant whose value is expected to be close to 0.5.

[60] The relationship between plume temperatures and power input Q was calibrated using experiments in a 0.6% glycerol - 0.4% cellulose solution. Measured axial temperature anomalies $\Delta T(z)$ are shown as a function of power input Q for two different heights above source (Figure C1).
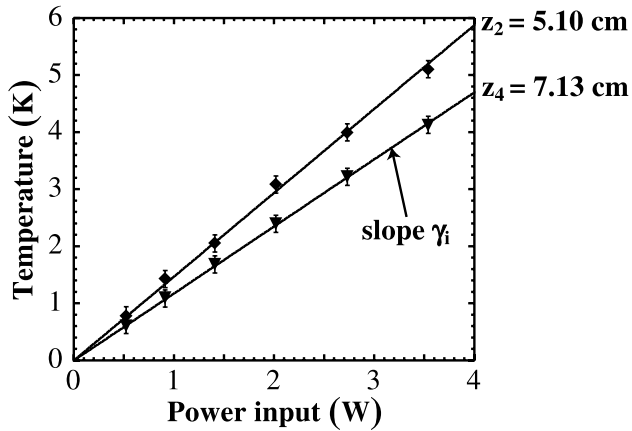
Figure C1. Axial temperature anomaly in experimental plumes as a function of power input for two different heights above source. Plume temperature is proportional to power input, as predicted by theory. Slope γ is used to determine the location of the virtual point source for the plume.

As expected, we find a linear relationship between temperature and power input:

$$\Delta T(z_i) \propto \gamma_i (Q - Q_0). \tag{C8}$$

For these experiments, power leakage Q_0 is negligible. According to scaling law (C7), parameter γ_i should be inversely proportional to the vertical distance above the virtual point source:

$$\frac{1}{\gamma_i} \propto z_i - z_0. \tag{C9}$$

As shown by Figure C2, the experimental data are consistent with this relationship and allow determination

of the virtual source depth z_0. For this particular experiment, $z_0 = -3.1 \pm 0.5$ cm and $C_e = 0.46 \pm 0.05$, which is in good agreement with the theoretical value of 0.5 for large Prandtl numbers [*Fujii*, 1963; *Worster*, 1986].

C3. Numerical Calculations

[61] As in the laboratory, numerical results can be described by a plume issuing from a virtual point source:

$$\Delta T(z) = C_n \frac{1}{2\pi\rho C_p \kappa} \frac{Q}{z - z_0}, \tag{C10}$$

where C_n is a constant and where we have used the fact there is no power leakage. Figure C3 shows the axial temperature anomaly as a function of time for three different grid sizes (64^3, 128^3, and 256^3).

[62] At given height above source, the temperature anomaly increases sharply as the plume head rises past that height, and then goes through a minimum before increasing again. The late increasing trend is due to the fact that the plume has risen to the top of the fluid, where it spreads horizontally. We therefore exclude this late phase for comparison with theory and use the minimum values as best estimates for an unbounded fluid layer. The absolute temperature anomaly in plume head and the temperature difference between head and conduit both decrease with increasing height above source. For all values of power input and heater size, constant C_n is very close to 0.5, the theoretical value from *Fujii* [1963] (Figure C4). Virtual source depth z_0 increases with heater size and power input, as one would expect on intuitive grounds.

[63] Numerical convergence is very good for absolute temperature values and only adequate as regards time evolution: results for the coarsest grid evolve about 15% faster than those for the finer grids. Such differences are largest for early times, when thermal boundary layers are very thin and hence difficult to handle numerically. For our purposes, this problem is not damaging because we are interested in fully developed plumes which impinge on the
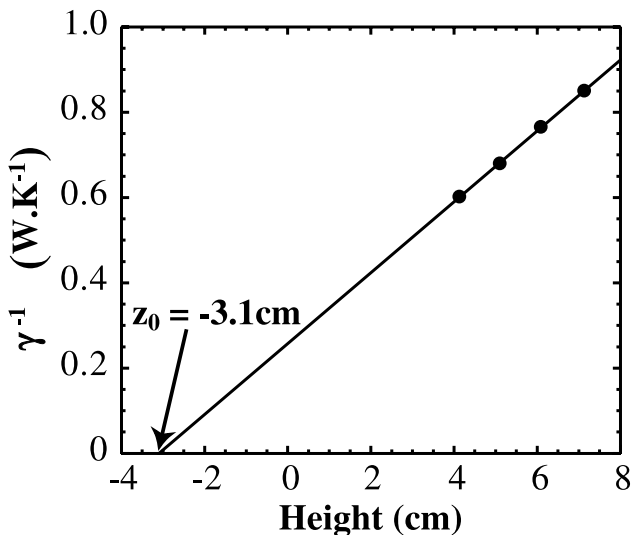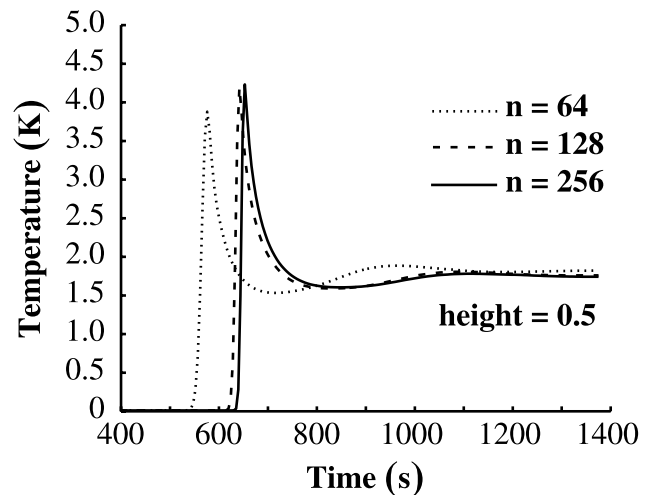

Figure C2. Plot of $1/\gamma$ as a function of height z. The zero intercept indicates the location of the virtual point source for the plume.

Figure C3. Axial temperature anomaly from numerical simulations as a function of time for three different grid sizes. Note that the largest grid size ($n = 64$) allows poor time resolution but good prediction of temperature values.
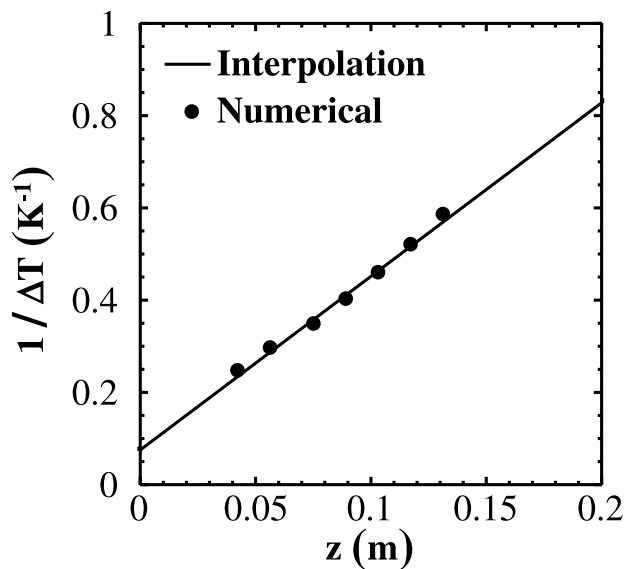
Figure C4. Axial temperature anomaly as a function of height z for one numerical simulation. The solid line corresponds to proportionality constant $C_n = 0.49$, close to the theoretical value for large Prandtl numbers.

upper layer. In such conditions, thermal anomalies are well developed over large radial distances.

[64] In these calculations, the short distance between source and interface does not allow accurate verification that the plume velocity does not depend on height z. However, the plume velocity is proportional to velocity scale W_B.

Notation

$\mathbf{v} = (u, v, w)$	local fluid velocity, m s^{-1}.
W	vertical velocity, m s^{-1}.
μ	viscosity, Pa s.
$\nu = \mu/\rho$	kinematic viscosity, m^2 s^{-1}.
α	thermal expansion, K^{-1}.
ρ	density, kg m^{-3}.
C_p	specific heat, J K^{-1} kg^{-1}.
κ	thermal diffusivity, m^2 s^{-1}.
$k = \rho C_p \kappa$	thermal conductivity.
$\sigma = \nu/\kappa$	Prandtl number.
Q	power input, W.

References

Albers, M., and U. R. Christensen (1996), The excess temperature of plume rising from the core-mantle boundary, *Geophys. Res. Lett.*, 23, 3567–3570.

Aulbach, S., W. Griffin, N. Pearson, S. O'Reilly, K. Kivi, and B. Doyle (2004), Mantle formation and evolution, Slave Craton: constraints from HSE abundances and Re-Os isotope systematics of sulfide inclusions in mantle xenocrysts, *Chem. Geol.*, 208, 61–88.

Bank, C.-G., M. Bostock, and R. M. Ellis (1998), Lithospheric mantle structure beneath the Trans-Hudson Orogen and the origin of diamondiferous kimberlites, *J. Geophys. Res.*, 103, 10,103–10,114.

Batchelor, G. K. (1954), Heat convection and buoyancy effects in fluids, *Q. J. R. Meteorol. Soc.*, 80, 339–358.

Boyd, F. R. (1989), Compositional distinction between oceanic and cratonic lithosphere, *Earth Planet. Sci. Lett.*, 96, 15–26.

Brand, R., and F. Lahey (1967), The heated laminar vertical jet, *J. Fluid Mech.*, 29, 305–315.

Cottrell, E., C. Jaupart, and P. Molnar (2004), Marginal stability of thick continental lithosphere, *Geophys. Res. Lett.*, 31, L18612, doi:10.1029/2004GL020332.

Couliette, D. L., and D. E. Loper (1995), Experimental, numerical and analytical models of mantle starting plumes, *Phys. Earth Planet. Inter.*, 92, 143–167.

Davaille, A., and C. Jaupart (1994), Onset of thermal convection in fluids with temperature-dependent viscosity: Application to the oceanic mantle, *J. Geophys. Res.*, 99, 19,853–19,866.

Doin, M.-P., L. Fleitout, and D. McKenzie (1996), Geoid anomalies and the structure of continental and oceanic lithospheres, *J. Geophys. Res.*, 101, 16,119–16,136.

Doin, M.-P., L. Fleitout, and U. Christensen (1997), Mantle convection and stability of depleted and undepleted continental lithosphere, *J. Geophys. Res.*, 102, 2771–2787.

Fouch, M. J., D. E. James, J. C. VanDecar, S. van der Lee, and the Kaapvaal Seismic Group (2004), Mantle seismic structure beneath the Kaapvaal and Zimbabwe cratons, *S. Afr. J. Geol.*, 107, 35–46.

Fujii, T. (1963), Theory of the steady laminar natural convection above a horizontal line heat source and a point heat source, *Int. J. Heat Mass Transfer*, 6, 597–606.

Griffin, W., S. O'Reilly, L. Natapov, and C. Ryan (2003), The evolution of lithospheric mantle beneath the Kalahari craton and its margins, *Lithos*, 71, 215–241.

Griffiths, R. W., and I. H. Campbell (1991), Interaction of mantle plume heads with the Earth's surface and onset of small-scale convection, *J. Geophys. Res.*, 96, 18,295–18,310.

Gung, Y., M. Panning, and B. Romanowicz (2003), Global anisotropy and the thickness of continents, *Nature*, 422, 707–711.

Hirth, G., and D. L. Kohlstedt (1996), Water in oceanic upper mantle: Implications for rheology, melt extraction and evolution of the lithosphere, *Earth Planet. Sci. Lett.*, 144, 93–108.

Huismans, R., Y. Podladchikov, and S. Cloetingh (2001), Transition from passive to active rifting: Relative importance of asthenospheric doming and passive extensive of the lithosphere, *J. Geophys. Res.*, 106, 11,271–11,291.

Jaupart, C., and J. C. Mareschal (1999), The thermal structure and thickness of continental roots, *Lithos*, 48, 93–114.

Jaupart, C., J. C. Mareschal, L. Guillou-Frottier, and A. Davaille (1998), Heat flow and thickness of the lithosphere in the Canadian Shield, *J. Geophys. Res.*, 103, 15,269–15,286.

Jellinek, A. M., and M. Manga (2004), Links between long-lived hot spots, mantle plumes D″, and plate tectonics, *Rev. Geophys.*, 42, RG3002, doi:10.1029/2003RG000144.

Kaminski, E., and C. Jaupart (2003), Laminar starting plumes in high-Prandtl-number fluids, *J. Fluid Mech.*, 478, 287–298.

Kerr, R. C., and C. Mériaux (2004), Structure and dynamics of sheared mantle plumes, *Geochem. Geophys. Geosyst.*, 5, Q12009, doi:10.1029/2004GC000749.

Kohlstedt, D. L., B. Evans, and S. J. Mackwell (1995), Strength of the lithosphere: Constraints imposed by laboratory experiments, *J. Geophys. Res.*, 100, 17,587–17,602.

Lebars, M., and A. Davaille (2004), Large interface deformation in two-layer thermal convection of miscible viscous fluids, *J. Fluid Mech.*, 499, 75–110.

Lenardic, A., and L.-N. Moresi (1999), Some thoughts on the stability of cratonic lithosphere: The effects of buoyancy and viscosity, *J. Geophys. Res.*, 104, 12,747–12,758.

Li, X., R. Kind, X. Yuan, I. Wölbern, and W. Hanka (2004), Rejuvenation of the lithosphere by the Hawaiian plume, *Nature*, 427, 827–829.

Moore, W. B., G. Schubert, and P. J. Tackley (1999), The role of rheology in lithospheric thinning by mantle plumes, *Geophys. Res. Lett.*, 26, 1073–1076.

Moresi, L.-N., and V. S. Solomatov (1995), Numerical investigation of 2d convection with extremely large viscosity variations, *Phys. Fluids*, 7, 2154–2162.

Morgan, J. P. (1997), The generation of a compositional lithosphere by mid-ocean ridge melting and its effect on subsequent off-axis hotspot upwelling and melting, *Earth Planet. Sci. Lett.*, 146, 213–232.

Morgan, W. J. (1971), Convection plumes in the lower mantle, *Nature*, 230, 42–43.

Moses, E., G. Zocchi, and A. Libchaber (1993), An experimental study of laminar plumes, *J. Fluid Mech.*, 251, 581–601.

Olson, P., G. Schubert, C. Anderson, and P. Goldman (1988), Plume formation and lithosphere erosion: A comparison of laboratory and numerical experiments, *J. Geophys. Res.*, *93*, 15,065–15,084.

Oxburgh, E., and E. Parmentier (1977), Compositional and density stratification in oceanic lithosphere—Causes and consequences, *J. Geol. Soc. London*, *133*, 343–355.

Parsons, B., and D. McKenzie (1978), Mantle convection and the thermal structure of the plates, *J. Geophys. Res.*, *83*, 4485–4495.

Poudjom-Djomani, Y. H., S. Y. O'Reilly, W. L. Griffin, and P. Morgan (2001), The density structure of subcontinental lithosphere through time, *Earth Planet. Sci. Lett.*, *184*, 605–621.

Ribe, N. M., and U. R. Christensen (1999), The dynamical origin of Hawaiian volcanism, *Earth Planet. Sci. Lett.*, *171*, 517–531.

Ribe, N. M., A. Davaille, and U. R. Christensen (2005), in *Mantle Plumes: A Multidisciplinary Approach*, edited by J. R. R. Ritter and U. R. Christensen, Springer, New York, in press.

Rondenay, S., M. G. Bostock, T. Hearn, D. J. White, and R. M. Ellis (2000), Lithospheric assembly and modification of the SE Canadian Shield: Abitibi-Grenville teleseismic experiment, *J. Geophys. Res.*, *105*, 13,735–13,754.

Rudnick, R. L., and A. A. Nyblade (1999), The thickness and heat production of archean lithosphere: Constraints from xenolith thermobarometry and surface heat flow, in *Mantle Petrology: Field Observations and High-Pressure Experimentation: A Tribute to Francis R. (Joe) Boyd*, edited by Y. Fei, C. M. Bertka, and B. O. Mysen, *Spec. Publ. Geochem. Soc.*, *6*, 3–12.

Sleep, N. H. (1990), Hotspots and mantle plumes: Some phenomenology, *J. Geophys. Res.*, *95*, 6715–6736.

Sleep, N. H. (1994), Lithospheric thinning by midplate mantle plumes and the thermal history of hot plume material ponded at sublithospheric depths, *J. Geophys. Res.*, *99*, 9327–9343.

Solomatov, V. S., and L.-N. Moresi (1997), Three regimes of mantle convection with non-Newtonian viscosity and stagnant lid convection on the terrestrial planets, *Geophys. Res. Lett.*, *24*, 1907–1910.

Solomatov, V. S., and L.-N. Moresi (2000), Scaling of time-dependent stagnant lid convection: Application to small-scale convection on Earth and other terrestrial planets, *J. Geophys. Res.*, *105*(B9), 21,795–21,818.

Tackley, P. J. (1994), Three-dimensional models of mantle convection: influence of phase transitions and temperature dependant viscosity, Ph.D. thesis, Calif. Inst. of Technol., Pasadena.

Tackley, P. J. (1996), Effects of strongly variable viscosity on three-dimensional compressible convection in planetary mantles, *J. Geophys. Res.*, *101*, 3311–3332.

Tackley, P. J., and S. D. King (2003), Testing the tracer ratio method for modeling active compositional fields in mantle convection simulations, *Geochem. Geophys. Geosyst.*, *4*(4), 8302, doi:10.1029/2001GC000214.

Tait, S., and C. Jaupart (1989), Compositional convection in viscous melts, *Nature*, *338*, 571–574.

Tait, S., and C. Jaupart (1992), Compositional convection in a reactive crystalline mush and melt differentiation, *J. Geophys. Res.*, *97*, 6735–6756.

Turner, J. S. (1973), *Buoyancy Effects in Fluids*, Cambridge Univ. Press, New York.

Turner, S., C. Hawkesworth, K. Gallagher, K. Stewart, D. Peate, and M. Mantovani (1996), Mantle plumes, flood basalts, and thermal models for melt generation beneath continents: Assessment of a conductive heating model and application to the Paraná, *J. Geophys. Res.*, *101*, 11,503–11,518.

van Keken, P. E., S. D. King, H. Schmeling, U. R. Christensen, D. Neumeister, and M.-P. Doin (1997), A comparison of methods for the modeling of thermochemical convection, *J. Geophys. Res.*, *102*, 22,477–22,495.

Vezolainen, A. V., V. S. Solomatov, J. W. Head, A. T. Basilevsky, and L.-N. Moresi (2003), Timing of formation of Beta Regio and its geodynamical implications, *J. Geophys. Res.*, *108*(E1), 5002, doi:10.1029/2002JE001889.

Wessel, P., and W. H. F. Smith (1991), Free software helps map and display data, *Eos Trans. AGU*, *72*, 441, 445–446.

White, R. S., and D. McKenzie (1989), Magmatism at rift zones: The generation of volcanic continental margins and flood basalts, *J. Geophys. Res.*, *94*, 7685–7729.

Worster, M. G. (1986), The axisymetric laminar plume: Asymptotic solution for large Prandtl number, *Stud. Appl. Maths*, *75*, 139–152.

————————————

G. Brandeis, C. Jaupart, and D. Jurine, Laboratoire de Dynamique des Systèmes Géologiques, Institut de Physique du Globe de Paris, 4 place Jussieu, F-75252 Paris Cedex 05, France. (jurine@ipgp.jussieu.fr)

P. J. Tackley, Department of Earth and Space Sciences, University of California, 3806 Geology Bldg., Los Angeles, CA 90095-1567, USA.